AAPS PharmSciTech (2026) 27:167
https://doi.org/10.1208/s12249-026-03353-2

RESEARCH ARTICLE

Albumin Nanoparticle-Based Delivery of Oxaliplatin-Oleic Acid Prodrug for Enhanced Breast Cancer Therapy

Oly Katari[1] · S. Lokesh[1] · Brojendra Nath Saren[1] · Vivek Yadav[1] · Kaushik Kuche[1] · Sanyog Jain[1]

Received: 1 November 2025 / Accepted: 20 January 2026

Abstract

Triple-negative breast cancer (TNBC) remains a therapeutic outlier, with limited targeted options and frequent relapse despite chemotherapy. While platinum therapy can benefit some TNBC cases, including BRCA1/2-mutant tumors, toxicity and limited tumor-selective exposure often restrict its impact. To address these barriers, we applied a lipid-metallodrug prodrug approach and synthesized an oxaliplatin-oleic acid (OXA-OA) conjugate that coupled OXA's cytotoxicity with OA-associated anticancer activity. The prodrug was encapsulated into genipin-crosslinked albumin nanoparticles (OXA-OA Alb NPs) to improve tumor targeting, yielding a uniform size of 140.52 ± 4.35 nm, a PDI of 0.25 ± 0.05, and an encapsulation efficiency of 84.55 ± 4.49%. Spectrometric analysis confirmed successful OXA-OA conjugation. The nanoparticles demonstrated enhanced cellular uptake and tumor targeting. *In vitro*, OXA-OA Alb NPs reduced the IC_{50} to 0.19 ± 0.36 µg/mL (4T1) and 0.20 ± 0.16 µg/mL (MDA-MB-231). This corresponded to 25 to 30-fold higher cytotoxicity than free OXA and > 50-fold than OA. Furthermore, apoptosis indices reached 1.47 (4T1) and 1.42 (MDA-MB-231), which were 4.19- and 4.50-fold higher than OA and 2.43- and 2.53-fold higher than OXA. *In vivo*, OXA-OA Alb NPs achieved ~ 90% tumor inhibition in a TNBC mouse model, with minimal systemic toxicity, stable liver and kidney function, and reduced organ damage compared with other treatment groups. These findings suggest that OXA-OA Alb NPs offer a promising and safer approach for TNBC, with potential for further exploration in preventing metastasis and recurrence.

Keywords Albumin nanoparticle · Oxaliplatin · Oleic acid · Prodrug · Triple-negative breast cancer

Introduction

TNBC remains one of the most clinically challenging forms of breast cancer. The absence of major hormonal receptors including estrogen (ER), progesterone (PR) and human epidermal growth factor receptor (HER2) reduces access to frontline targeted regimens [1]. Chemotherapy therefore remains a treatment backbone, but dose-limiting toxicities and limited durability continue to pose long-term challenges [2]. Being biologically heterogeneous, TNBC also comprises distinct molecular subtypes with diverse genomic alterations and evolving transcriptional states. While this complexity may seem like a barrier, it offers a strategic roadmap to actionable vulnerabilities as well. A key example is BRCA1/2-associated repair deficiency, which can increase susceptibility to platinum-induced DNA lesions [3]. Oxaliplatin (OXA), originally approved for metastatic colorectal cancer, has therefore attracted renewed interest in breast cancer research, including TNBC. OXA exerts cytotoxicity by forming DNA adducts that interfere with replication and transcription [4, 5]. However, the clinical utility of OXA in TNBC is limited by several pharmacological and safety concerns. Its hydrophilic nature contributes to rapid systemic clearance and poor tumor accumulation, while its broad biodistribution leads to dose-limiting toxicities, particularly peripheral neuropathy. These adverse effects often necessitate dose reduction or early discontinuation, compromising therapeutic efficacy [6]. To overcome these barriers, platinum(IV) (Pt(IV)) prodrugs have emerged as a promising platform. Unlike the square-planar Pt(II) configuration of OXA, Pt(IV) complexes adopt an octahedral

Oly Katari and S. Lokesh deserve as first author.

✉ Sanyog Jain
sanyogjain@niper.ac.in; sanyogjain@rediffmail.com

[1] Centre for Pharmaceutical Nanotechnology, Department of Pharmaceutics, National Institute of Pharmaceutical Education and Research (NIPER), S.A.S. Nagar, Sector 67, Mohali, Punjab 160062, India

Published online: 02 April 2026

geometry, offering two axial positions that can be functionalized to fine-tune their properties. Among the various ligand strategies, long-chain fatty acids such as palmitic and stearic acids have been proposed to modify Pt(IV) prodrugs. These modifications are intended to enhance lipophilicity, promote membrane interaction, and even exploit fatty acid transporter-mediated uptake. For example, Zheng *et al.* showed that a cisplatin-derived Pt(IV) bearing a C_{16} alkyl chain forms a 1:1 complex with serum albumin, burying the complex beneath the protein surface and greatly slowing its reduction in blood [7]. Other Pt(IV)-fatty acid complexes such as bis(octanoato)(Pt(IV)) and bis(laurato)(Pt(IV)) have shown strong activity against cisplatin-resistant ovarian cancer cells [8]. These Pt(IV)-fatty acid conjugates illustrate the value of lipophilic prodrugs: they can evade the normal copper transporter (Ctr1) uptake pathway and kill resistant cells. However, most Pt(IV)-fatty acid conjugates to date rely on saturated fatty acids, which function primarily as solubility modifiers. In contrast, oleic acid (OA), a monounsaturated fatty acid, exhibits dual functionality, serving as a lipophilic modifier while also acting as a biologically active agent. Several studies have shown that OA induces apoptosis via multiple mechanisms, including oxidative stress and disruption of oncogenic signaling pathways such as FAK/AKT/NF-κB [9], EGFR/ERK/AP-1 [10], PLD/Cdc42 signaling [11]. OA has also been linked to AKT/mTOR suppression and PTEN enhancement, converging on mitochondrial dysfunction and caspase-dependent death programs [12, 13]. Nevertheless, the cellular uptake of OA has been found to be poor at physiological pH due to its anionic nature, often requiring greater exposure to elicit an effect [14, 15]. Many Pt(IV)-fatty acid prodrugs likewise show low bioavailability and unpredictable tumor targeting driven by passive/protein-mediated transport, with added risk of aggregation/precipitation [7]. Therefore, a nano-enabled delivery platform offers a practical solution.

Albumin (Alb), a protein naturally abundant in the body, offers remarkable advantages as a drug delivery system due to its inherent biocompatibility, prolonged circulation time, and tumor-targeting capabilities [16]. It possesses natural binding sites that enable it to interact with specific receptors such as gp60, SPARC and FcRn, promoting its accumulation in tumor tissues through receptor-mediated endocytosis [17]. To date, several Alb-based products have been developed and approved by the FDA, including Abraxane® and Fyarro® [18]. Accordingly, covalent Alb-binding Pt(IV) prodrugs have been developed to harness Alb's long circulation time and tumor-homing properties. For example, Schueffl *et al.* designed KP2156, a maleimide-containing oxaliplatin(IV) complex that rapidly and stably binds the free thiol of Alb in blood [19]. KP2156 dramatically prolongs plasma half-life and "enhances the effective platinum dose" delivered to the tumor. However, these approaches often rely on non-specific *in situ* Alb conjugation, which can result in low drug loading and limited control over nanoparticle size and release behavior. Another class of systems combines lipids and Alb. In "lipid-albumin nanoparticles" (LANs), Alb is formulated alongside lipid components to deliver therapeutics such as nucleic acids. For instance, Li *et al.* constructed LANs using a cationic human serum albumin-polyethyleneamine conjugate and lipid (DOTAP/soyPC) to deliver an antisense oligonucleotide against HIF-1α. These LANs showed significantly greater uptake and gene silencing in tumor cells than lipid-only nanoparticles, and in mouse xenografts they markedly reduced tumor HIF-1α and extended survival [20]. A folate-targeted variant (F-LAN) delivered an Akt1 antisense to KB carcinoma, where the Alb-containing nanoparticle achieved longer circulation time and greater tumor inhibition than lipid nanoparticles at equivalent dose [21]. Although promising in macromolecular drug delivery, these hybrid systems remain underexplored for small-molecule Pt(IV) chemotherapeutics.

Herein, we present a rationally designed dual-functional platform in which OXA is axially conjugated to oleic acid (OXA-OA) and encapsulated into genipin-crosslinked albumin nanoparticles (OXA-OA Alb NPs). This approach integrates the bioactivity and lipophilicity of OA with the biocompatibility, tumor-targeting capacity, and solubilization potential of Alb. Unlike prior fatty acid-Pt(IV) conjugates that depend solely on lipid modification or passive serum protein binding, our strategy uses Alb as a direct nanocarrier to improve colloidal stability, optimize particle size, and enable both passive and active tumor targeting. The OXA-OA Alb NPs are designed to remain stable during circulation and accumulate in tumor tissues, where elevated intracellular glutathione levels facilitate prodrug reduction and release of active OXA. We synthesized and characterized the OXA-OA prodrug and its Alb-encapsulated form, and systematically evaluated their cellular uptake, cytotoxicity, and antitumor efficacy in TNBC models. Our findings demonstrate that this platform not only enhances therapeutic potency but also reduces systemic toxicity, offering a promising and clinically translatable approach for the targeted treatment of TNBC.

Materials and Methods

Materials

OXA was generously provided by Cipla Ltd. (India). Oleic anhydride and glutaraldehyde were purchased from TCI Chemicals (India), and bovine serum albumin was obtained from HiMedia Laboratories (India). Genipin, Coumarin-6, the Annexin V-FITC apoptosis detection kit and MTT

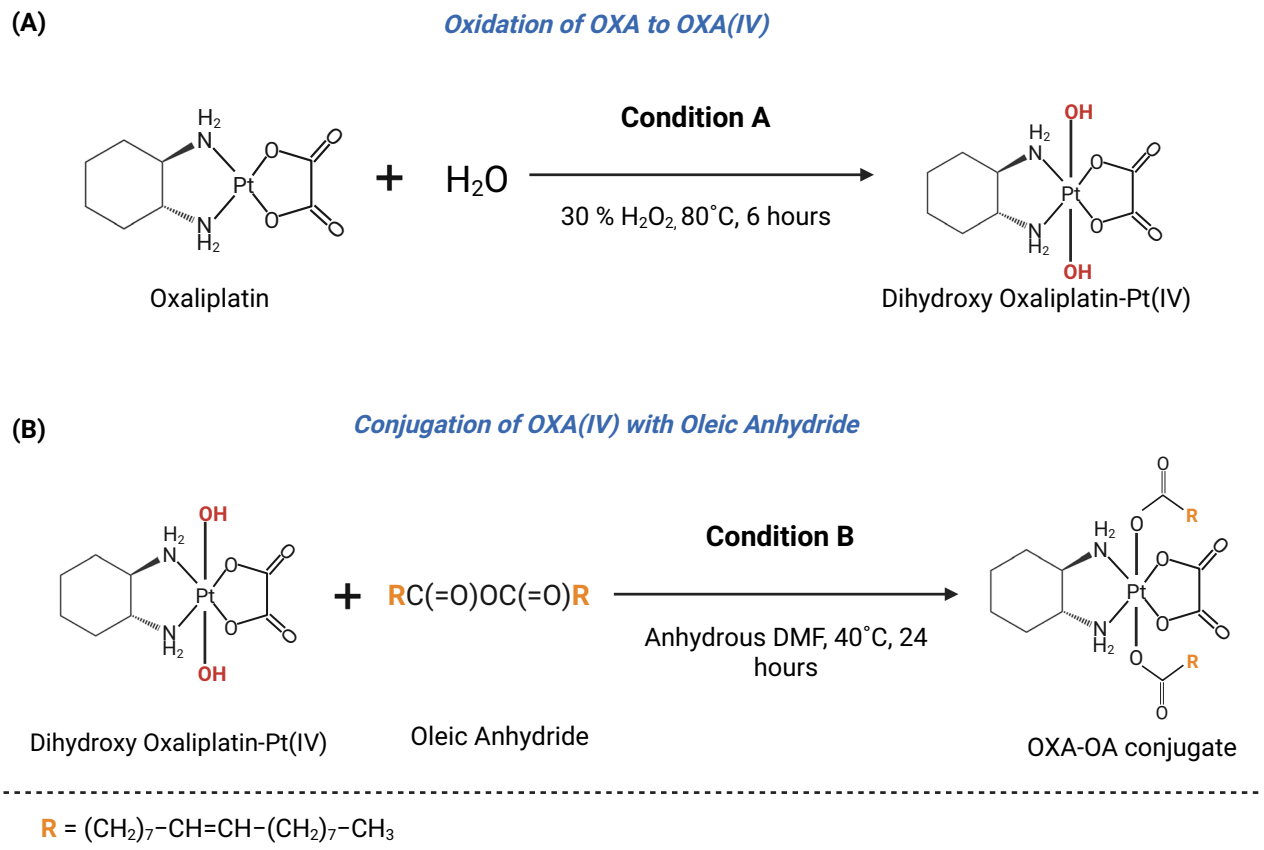

Fig. 1 Schematic representation of the synthesis of OXA-OA conjugate

reagent were sourced from Sigma-Aldrich (India). Cell-culture reagents, including DPBS and trypsin–EDTA, were obtained from Thermo Fisher Scientific (USA). Unless otherwise stated, all chemicals were of analytical grade and procured from local suppliers.

Synthesis of OXA-OA

To enable axial-ligand conjugation, OXA was first oxidized to its Pt(IV) intermediate and then coupled with oleic anhydride to yield the OXA-OA conjugate, following reported procedures with minor operational adaptation [22, 23]. Initially, OXA (40 mg) was dissolved in water (2 mL), 30% (w/v) aqueous H_2O_2 was added, and the reaction was stirred at 200 rpm for 6 h at 80°C under light-protected conditions to generate the OXA(IV) intermediate. The resulting product was lyophilized to obtain a crystalline intermediate for the subsequent step. For conjugation, the intermediate (1 mol equivalent) was reacted with oleic anhydride (3 mol equivalents) in anhydrous DMF and stirred at 40°C for 24 h. The reaction was quenched by addition of excess ice-cold water, and the product was extracted sequentially with dichloromethane, diethyl ether, and ethyl acetate. The combined organic layers were pooled, dried over anhydrous sodium sulfate, and concentrated under reduced pressure. The resulting oily conjugate was further dried in a vacuum oven to remove residual solvents. Formation of OXA-OA was confirmed by ^{1}H NMR, ^{13}C NMR, High-resolution mass spectrometry (HRMS) and FTIR. The detailed reaction conditions and schematic representation are provided in the Fig. 1.

Determination of Partition Coefficient

The partition coefficient (Log P) of OXA and OXA-OA was assessed using an octanol–water partitioning method, following a previously established protocol [24]. Briefly, OXA (5 mg) and OXA-OA (5 mg) were dissolved in DMF and introduced into a pre-equilibrated biphasic system containing *n*-octanol and PBS (pH 7.4) at a 1:1 (v/v) ratio. The mixture was shaken at 37°C for 12 h to allow equilibration between phases. After equilibration, the phases were separated by centrifugation (7,000 rpm, 10 min), and the aqueous phase was collected. The analyte concentration in the aqueous phase was quantified by HPLC on a Shimadzu® system equipped with a PDA detector and a reversed-phase C18 column (LiChrospher® 100 RP-18, 5 µm). OXA was analyzed under isocratic conditions using acetonitrile:water (5:95, pH

3.0) at 0.8 mL/min with detection at 210 nm ($t_R \approx 7.3$ min), whereas OXA-OA was analyzed using methanol:water (98:2, pH 4.0) at 1.0 mL/min with detection at 218 nm ($t_R \approx 8.5$ min). For additional details on chromatographic conditions and calibration, please refer to the Supplementary file. The amount in the octanol phase was calculated by mass balance, and Log P was computed as:

$$\text{Log P} = \text{Log}_{10}\left(\frac{C_{Octanol}}{C_{Aqueous}}\right)$$

Reduction Behavior of OXA-OA

The reduction profile of OXA-OA was determined by following a previously reported method [24], designed to mimic physiologically relevant and reductive microenvironments. Briefly, OXA-OA was incubated in three media: PBS (pH 7.4) alone (control), PBS containing L-ascorbate (400 µM), and PBS containing glutathione (GSH, 400 µM). The mixtures were maintained at 37°C under gentle stirring for 12 h. At 2 h intervals, aliquots (200 µL) were withdrawn and immediately subjected to octanol partitioning to separate unreduced conjugate from released hydrophilic drug. The samples were vortexed for 15 min and centrifuged to achieve clear phase separation, after which the aqueous phase was collected and analyzed by HPLC to quantify liberated OXA. The presence of free OXA after reduction was further verified by mass spectrometry.

Estimation of Reduction Half-Life

The reduction time-course data were used to estimate the reduction half-life ($t_{1/2}$) of OXA-OA in both L-ascorbate and GSH media. For each condition, plots of $\ln(C_t/C_0)$ *versus* time were constructed, and the linear fit was found to be consistent with pseudo-first-order reduction kinetics. The reaction rate constant (k) was obtained from the slope, and $t_{1/2}$ was calculated using the standard relationships: $C_t = C_0 e^{-kt}$ and $t_{1/2} = 0.693/k$, where C_0 and C_t represent the drug concentrations at time 0 and time t, respectively [24].

Development of OXA-OA Alb NPs

Preparation and Optimization of OXA-OA Alb NPs

OXA-OA Alb NPs were prepared by a desolvation-based approach as previously described [23]. Briefly, Alb (25 mg) was dissolved in 10 mM NaCl (1 mL) and the solution was filtered to remove any particulates. The pH was then adjusted to 8–9 using 0.1 M NaOH to favor NPs formation and subsequent crosslinking. Separately, the OXA-OA conjugate was dissolved in methanol and added dropwise to the Alb solution under stirring. Ethanol was then introduced as the desolvating agent to induce NPs formation, and the endpoint was identified by the appearance of uniform turbidity. The resulting dispersion was stabilized by adding genipin as the crosslinker, followed by continuous stirring for 24 h to allow crosslinking to proceed. The optimized formulation was subsequently lyophilized and stored for further use. The same preparation approach was used to prepare C-6 loaded Alb NPs for cellular uptake studies.

Crosslinking Efficiency and Time

Genipin-mediated Alb crosslinking was quantified by fluorescamine-based measurement of residual primary amines using a Nanodrop 3300® fluorospectrometer (Thermo Fisher Scientific). Briefly, lyophilized genipin-crosslinked Alb NPs (Gen Alb NPs; 5 mg) were dispersed in PBS (pH 7.4, 1 mL). At each time point (4, 8, 12, and 24 h), an aliquot (9 µL) was withdrawn and immediately mixed with fluorescamine (3 µL; 3 mg/mL in DMSO). The reaction mixtures were incubated at room temperature for 15 min, briefly centrifuged to remove any particulates, and the fluorescence signal was recorded. The crosslinking time was determined in terms of Relative Fluorescent Units (RFU) using the following equation:

$$\%\ \text{Amino groups consumed} = \frac{\text{RFU}_{\text{Alb NPs}} - \text{RFU}_{\text{Alb Crosslinked}}}{\text{RFU}_{\text{Alb NPs}}} \times 100$$

Characterization of OXA-OA Alb NPs

Particle Size, Shape and Morphology

The optimized OXA-OA Alb NPs were characterized for hydrodynamic diameter, polydispersity index (PDI) and zeta potential using Zetasizer (ZS 3000; Malvern Instruments, UK). Particle morphology was examined by transmission electron microscopy (TEM; FEI Tecnai G2F20, Netherlands). The detailed method is described in the supplementary file.

Determination of Drug Loading and Entrapment Efficiency

Association of conjugate with Alb NPs was quantified by an indirect method [25]. Briefly, the OXA-OA Alb NPs dispersion was centrifuged (5,000 rpm, 5 min) to separate unbound OXA-OA, which precipitated under these conditions. The pellet containing the unbound conjugate was then dissolved in methanol and quantified by using a validated HPLC method. The amount of bound OXA-OA was determined

by subtracting the unbound fraction from the total amount of conjugate initially added.

Circular Dichroism (CD) Spectroscopy

CD spectroscopy was performed to examine whether genipin crosslinking altered the secondary structure of Alb. Samples of native Alb and Gen Alb NPs were prepared at 0.2 mg/mL in 10 mM NaCl, as previously reported [26]. Far-UV CD spectra were collected from 190 to 260 nm using a J-810 spectropolarimeter (Jasco, Tokyo, Japan) with a 0.1 cm path-length quartz cuvette. For comparative purposes, the CD analysis was also performed for glutaraldehyde-crosslinked Alb NPs (Glu Alb NPs; 0.8% w/v), a conventional crosslinker widely utilized particularly for creating stable Alb NPs [27]. Spectral overlays were evaluated to assess changes in α-helical signatures and overall structural integrity following crosslinking.

Lyophilization

To improve storage stability, the optimized OXA-OA Alb NPs were lyophilized using a VirTis Wizard 2.0 freeze-dryer (VirTis, New York, USA) following a previously reported stepwise freeze-drying cycle [28]. Accordingly, mannitol, sucrose, dextrose, and trehalose were evaluated as lyoprotectants at different concentrations (1–10% w/v). For each condition, formulation aliquots (~2 mL) were dispensed into glass vials and subjected to freeze-drying using the established lyophilization cycle (Table S2). Thereafter, the freeze-dried cakes were stored at −20°C until further use. For redispersibility assessment, dried cakes were rehydrated in PBS (pH 7.4) to the original volume with gentle vortexing, and cake appearance and reconstitution time were recorded. Finally, the hydrodynamic diameter and PDI were measured by DLS to calculate S_f/S_i (S_f, size after reconstitution; S_i, size before lyophilization). For additional methodological details, please refer to the Supplementary file.

In Vitro Drug Release Analysis

In vitro release studies were carried out to compare the release of conjugate from the optimized formulation under physiological and acidic conditions. Briefly, samples were loaded into cellulose dialysis tubing (MWCO 14 kDa) and dialyzed against 20 mL of release medium, as previously described [29]. Release was carried out in PBS (pH 7.4) and acetate buffer (pH 5.5), with the system maintained at 37 ± 0.5°C in a shaker water bath (80 strokes/min). At predetermined time points (0.5, 1, 2, 3, 6, 12, 24, and 48 h), 1 mL aliquots were withdrawn and replaced with an equal volume of fresh medium to maintain sink conditions. The amount of released conjugate was quantified by HPLC using the validated method.

In Vitro Hemolytic Study

Hemolytic compatibility of the developed formulation was assessed using fresh blood collected from Sprague Dawley rats. The assay was performed following a previously reported protocol [22]. Full experimental details, including sample preparation and calculation of percent hemolysis, are provided in the Supplementary file.

In Vitro cell line-based experiments

Cells

Cell-based studies were performed using 4T1 cells (ATCC, Manassas, VA, USA) and MDA-MB-231 cells (NCCS, Pune, India). Cells were cultured under standard conditions as described previously [30], and the recommended media, supplements, and incubation settings for each cell line were maintained throughout the experiments.

Qualitative Estimation of Cellular Uptake

Qualitative uptake was examined in 4T1 and MDA-MB-231 cells using coumarin-6 (C6) as a model fluorophore to visualize cellular internalization by fluorescence imaging. Initially, the cells were seeded in 6-well plates (Corning Costar, NY, USA) at 5×10^4 cells/well and allowed to attach overnight. C-6 loaded Alb NPs were prepared using the same procedure as OXA-OA Alb NPs, substituting C-6 for OXA-OA. Cells were then incubated with free C-6 solution or C-6 loaded Alb NPs (equivalent to 1 µg/mL C-6) for 3 h, following the previously described qualitative uptake procedure [30]. After incubation, the medium was removed and cells were washed three times with DPBS (pH 7.4), fixed with 2.5% (v/v) glutaraldehyde, and imaged using a confocal laser scanning microscope (CLSM; Olympus FV1000).

Quantitative Estimation of Cellular Uptake

For quantification, 4T1 and MDA-MB-231 cells were seeded at 1×10^5 cells/well in 6-well plates and incubated with OXA-OA Alb NPs (10 µg/mL, expressed as OXA-OA equivalent) for 0.5, 1, 2, or 3 h. At each time point, cells were washed three times with PBS to remove extracellular material, then permeabilized with 0.1% (v/v) Triton X-100 and extracted with methanol to recover internalized drug, as reported previously [22]. The lysate was then centrifuged

(10,000 rpm, 10 min, 4°C; Sigma K300, USA), and the supernatant was analyzed by HPLC for intracellular drug quantification using the established method.

Cell Viability Assay

Cell viability was evaluated in 4T1 and MDA-MB-231 cells using the MTT assay. The experiment was performed according to a previously reported protocol [22], and the full procedure is provided in the supplementary file.

Annexin V Apoptosis assay

For apoptosis assessment, MDA-MB-231 cells were seeded in 6-well plates (1×10^5 cells/well; Costar, Corning Inc.) and allowed to attach overnight at 37°C in 5% CO_2. After treatment with the formulations, cells were stained using an Annexin V-Cy3.18/6-carboxyfluorescein diacetate (6-CFDA) dual-label protocol to capture phosphatidylserine externalization and membrane integrity. Stained cells were imaged by CLSM using the green channel (6-CFDA) and red channel (Annexin V-Cy3.18). Green-only cells were classified as viable, dual-positive (green + red) cells as apoptotic, and red-only cells as necrotic. An apoptosis index was calculated as the red-to-green fluorescence intensity ratio, and fluorescence intensities were quantified from CLSM images using ImageJ software (NIH, USA).

In Vivo Animal Study

All the animal study protocols were duly approved by the Institutional Animal Ethics Committee (IAEC) (Approval No. IAEC/23/79) and were conducted in compliance with CPCSEA (India) guidelines.

Anticancer Efficacy Study

The *in vivo* anticancer activity of free OXA, OXA-OA, and OXA-OA Alb NPs was assessed in an orthotopic 4T1 TNBC model in female BALB/c mice. Female BALB/c mice (6–8 weeks old, 20–25 g) were obtained from an accredited animal facility. 4T1 cells were cultured to 80–90% confluence, harvested, and resuspended in PBS; 1×10^6 cells in 100 µL were injected into the mammary fat pad to establish tumors. When tumors became palpable and reached ~ 100 mm^3, animals were randomized into four treatment groups (n = 3 per group). Formulations were administered intravenously at an OXA-equivalent dose of 5 mg/kg on an every-four-days schedule.

Tumor volumes (external) were measured every alternate day using digital calipers and calculated using the formula:

$$Tumor\ volume\ (mm^3) = \frac{Length \times (Width)^2}{2}$$

where length and width represent the largest and smallest dimensions of the tumor, respectively. At the end of the study, mice were euthanized, and tumors were excised and weighed to determine tumor weight. % Tumor burden was then calculated as a percentage of body weight using the following formula:

$$\%\ Tumor\ burden = \frac{\text{Weight of the tumor}}{\text{Total body weight of the animal}} \times 100$$

The therapeutic impact was further quantified by calculating the tumor inhibition rate (TIR), which provides a direct comparison of tumor suppression between treatment and control groups:

$$\%Tumor\ inhibition\ rate = \left(1 - \frac{\text{Tumor volume}_{(\text{Treated})}}{\text{Tumor volume}_{(\text{Control})}}\right) \times 100$$

Toxicity Study

To evaluate the systemic toxicity of OXA-OA Alb NPs, healthy Swiss albino mice (20–25 g) were randomly divided into four groups (n = 5 per group). The treatment groups received formulations at a drug-equivalent dose of 5 mg/kg on an every-4-days schedule for 21 days, while the control group received normal saline [31].

Blood Biochemistry

Following the study's completion, venous blood samples were drawn from the subjects for comprehensive biochemical evaluation. This analysis focused on assessing key indicators of liver and kidney function, including the enzymes aspartate aminotransferase (AST), alanine aminotransferase (ALT), blood urea nitrogen (BUN) as well as creatinine levels. These evaluations were specifically conducted to assess the physiological effects and potential toxicity associated with the administered NPs compared to the free OXA and OXA-OA. Analyses were performed using certified commercial diagnostic kits (AccuRex Biomedical Pvt. Ltd., India) according to the manufacturer's instructions.

Organ Histopathology

For histopathological evaluation, major organs (liver, kidney, spleen, lung, and heart) were collected from treated animals and immediately fixed in 10% neutral-buffered formalin. Tissues were then processed, paraffin-embedded, and sectioned (4–5 µm). Sections were mounted on glass slides and stained

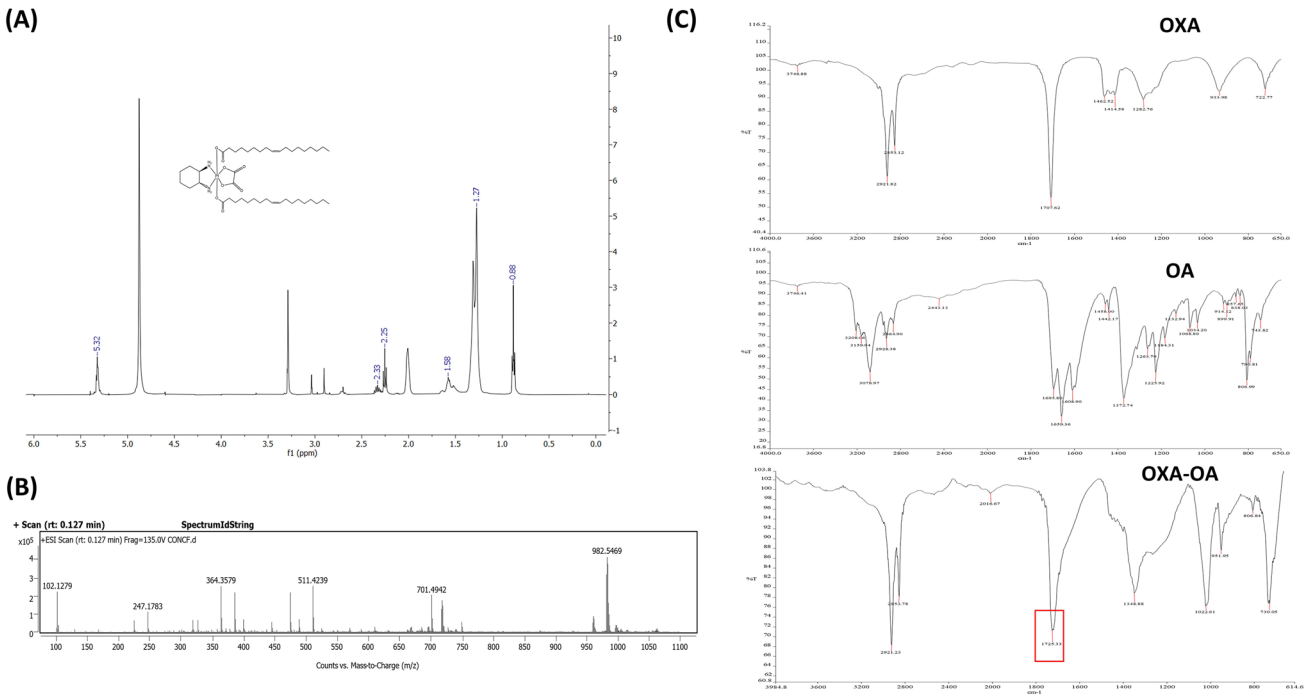

Fig. 2 Structural characterization of the OXA-OA: (**A**) spectral confirmation comprising (i) ^{1}H-NMR (400MHz, DMSO) spectrum in DMSO-d_6 of OXA-OA—5.32 (m, 4H, -CH = CH-), 2.25 (t, 2H, -CH2CO-), 2.11 (m, 8H, -CH2CH = CHCH2-), 2.01 (d, 10H, hexamethylene), 1.27 (m, 40H, -CH2CH2CH2-), 0.88 (t, 6H, -CH2CH3); (**B**) Mass spectrum of OXA-OA; (**C**) FTIR spectra of OXA, OA and OXA-OA

with hematoxylin and eosin (H&E) to visualize overall tissue architecture. The stained slides were examined under a light microscope for morphological alterations and any treatment-associated pathological changes.

Statistical Analysis

Data were expressed as mean ± SD. Statistical analyses were performed using GraphPad InStat® (GraphPad Software, CA, USA). One-way or two-way ANOVA was applied as appropriate; Tukey–Kramer's multiple-comparisons test was used after one-way ANOVA, and Bonferroni post-tests were used after two-way ANOVA to compare group means. Differences were considered statistically significant at $p < 0.05$.

Results and Discussion

OXA-OA Characterization

Successful formation of the OXA-OA conjugate was confirmed through a series of analytical techniques, including ^{1}H NMR, ^{13}C NMR, mass spectrometry and FTIR spectroscopy.

^{1}H NMR Spectroscopy

^{1}H NMR spectroscopy provided clear evidence for successful conjugation of OXA with OA. In the spectrum of the conjugate, a characteristic signal was observed in the δ 2.1–2.3 ppm region, corresponding to the α-methylene (-CH_2-) protons adjacent to the carbonyl group of OA (Fig. 2A). Compared with free OA, this α-methylene resonance shifted from δ 2.34 ppm to δ 2.25 ppm after conjugation, consistent with a changed electronic environment upon coupling. This downfield/upfield movement supports formation of the intended ester linkage between the hydroxyl functionality of the OXA(IV) intermediate and the OA-derived carbonyl. Moreover, ^{13}C NMR analysis showed a distinct carbonyl resonance at δ 178.6 ppm, consistent with an ester carbonyl, providing additional support for ester bond formation. (Please refer to the supplementary material).

HRMS (High-Resolution Mass Spectrometry)

HRMS further supported formation of the OXA-OA conjugate by confirming the expected molecular mass. The spectrum showed a dominant ion at m/z = 982.54 (Fig. 2B), which corresponds to the sodium adduct $[M+Na]^+$ of the conjugate. The calculated monoisotopic mass for the sodium adducts ($C_{44}H_{78}N_2O_8Pt$) was 983.20 Da and was in close

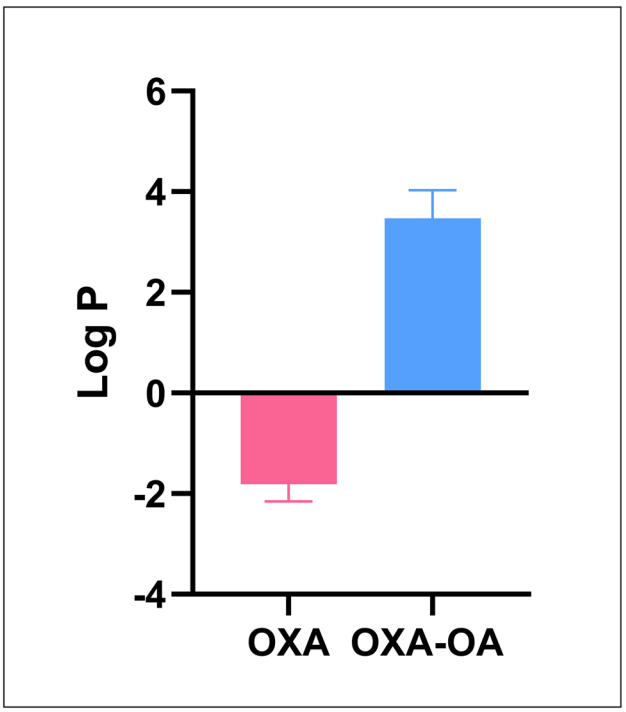

Fig. 3 Log P of OXA and OXA-OA

agreement with the experimental value. In addition, lower-m/z fragment ions (e.g., m/z 701.49, 511.42, and 364.35) were observed, consistent with in-source fragmentation and ligand/side-chain cleavage under electrospray ionization conditions, including loss of oleate-associated fragments.

FTIR Spectroscopy

FTIR analysis provided complementary evidence consistent with ester formation between OXA and OA. The conjugate exhibited a distinct absorption band at 1725.33 cm^{-1}, consistent with ester C = O stretching. Figure 2C. Compared with free OA, where the carbonyl stretch was typically observed near ~ 1707 cm^{-1}, this shift was consistent with esterification of the OA carbonyl in the conjugate [32]. Additionally, the absorption bands at 2920 cm^{-1} and 2853 cm^{-1}, assigned to aliphatic C-H stretching, further supported retention of the long-chain OA moiety within the OXA-OA structure.

Determination of Partition Coefficient

OA conjugation markedly altered the hydrophilic-lipophilic balance of OXA. The OXA-OA conjugate showed a Log P of 3.47 ± 0.56, representing a pronounced shift from native OXA (Log P − 1.81 ± 0.34) [33] (Fig. 3). This marked increase in lipophilicity supported the design rationale by suggesting improved membrane partitioning and reduced dependence on aqueous solubility relative to free OXA. Consistent with this profile, OXA-OA was well suited for incorporation into protein-based nanocarriers, where increased hydrophobicity can favor efficient encapsulation and more controlled payload presentation.

Reduction Behavior of OXA-OA Conjugate

Because Pt(IV) complexes are designed as prodrugs, their therapeutic activity is expected to emerge only after intracellular reduction to the corresponding Pt(II) species. Pt(IV) derivatives (d^6, octahedral) are typically more kinetically inert than Pt(II) and therefore remain comparatively stable in extracellular fluids, while being reducible in the cytosol where endogenous reductants such as GSH and ascorbate are present at much higher concentrations than in plasma [34, 35]. In line with this design principle, OXA-OA remained stable in PBS (pH 7.4) with negligible change over 12 h (Fig. 4A) [36]. In contrast, reduction proceeded rapidly in the presence of biologically relevant reductants: within 2 h, ~ 90% of the OXA(IV) fraction was reduced in GSH (≈10% remaining), whereas ascorbate produced ~ 80% reduction over the same interval. Continued incubation further decreased the OXA(IV) fraction, approaching near-complete conversion by 12 h in both conditions, with GSH consistently showing faster reduction kinetics than ascorbate. Mass spectrometry (Fig. 4B) showed the emergence of a new Pt-containing signal centered at ~ m/z 475 following incubation with reductants [37]. The higher efficiency of GSH likely reflects its thiol nucleophile, which can more readily access and reduce the OXA(IV) center; the amphiphilic OA moiety on the conjugate may further facilitate such interactions. Ascorbate, lacking a thiol, donates electrons via hydroxyl groups and is correspondingly less reactive under these conditions [34, 38].

Reduction Kinetics of OXA(IV)

To assess how rapidly the OXA-OA prodrug could be activated under biologically relevant reductive conditions, we analyzed reduction kinetics in GSH and ascorbic acid by plotting $\ln(C_t/C_0)$ *versus* time and fitting the data by linear regression Fig. 4C&D. The rate constant (k) was obtained from the slope, and half-life was calculated using $t_{1/2} = 0.693/k$. The calculated half-lives were 2.83 ± 0.18 h in GSH and 3.06 ± 0.22 h in ascorbic acid (n = 3), as summarized in Fig. 4E. In line with the expected thiol-driven activation behavior, the conjugate was reduced slightly faster in GSH than in ascorbic acid. In biological terms, this preference is meaningful because GSH is strongly compartmentalized, typically ~ 1–10 mM (*vs* ~ 2–20 µM in plasma/extracellular compartments) [39]. Accordingly, reduction is expected to be favored after cellular uptake rather than in circulation. Notably, TNBC cell

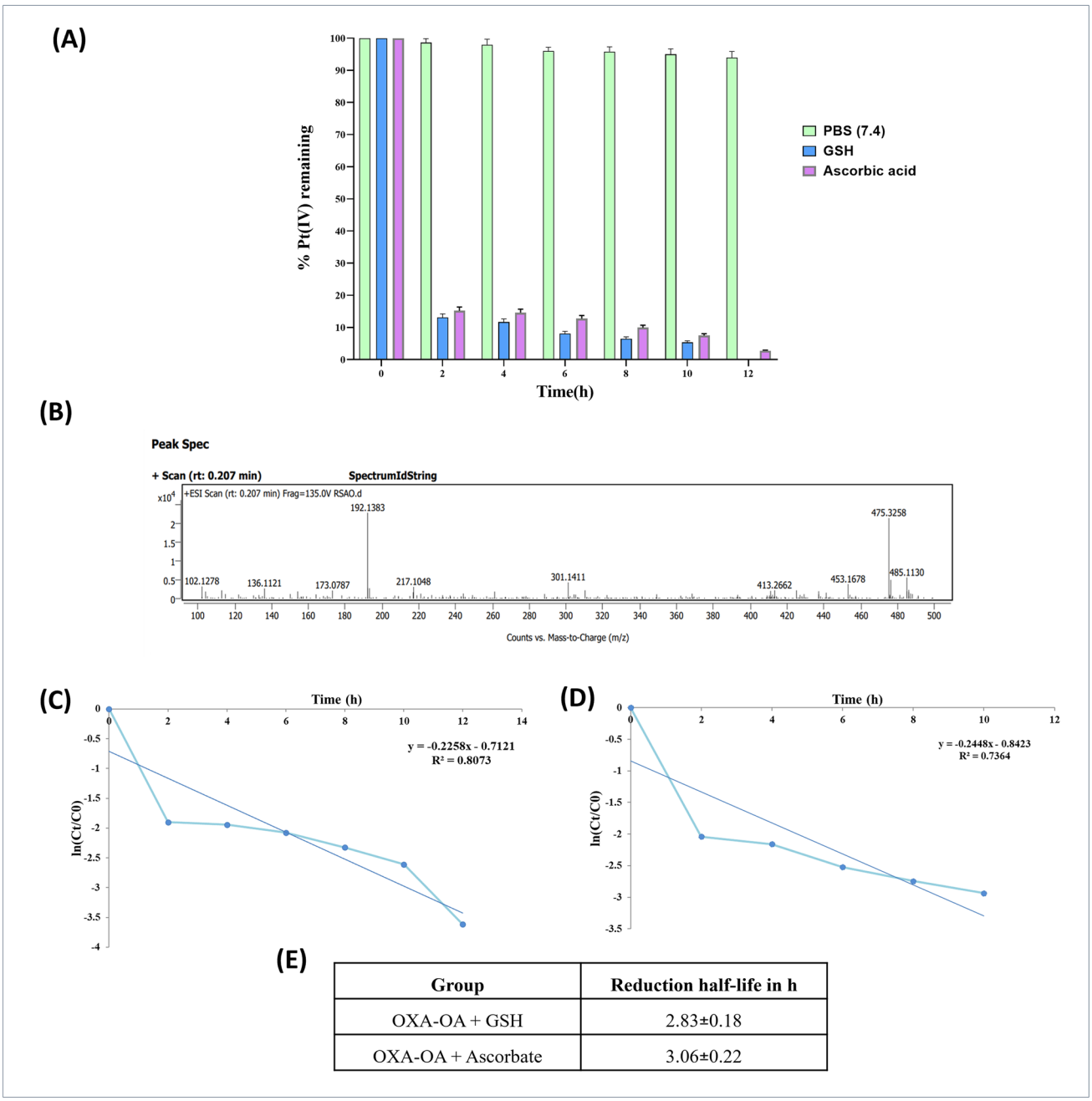

(E)

Group	Reduction half-life in h
OXA-OA + GSH	2.83±0.18
OXA-OA + Ascorbate	3.06±0.22

Fig. 4 Stability and reductive conversion of OXA-OA with kinetic analysis: Reduction studies comprising (**A**) percentage of OXA-OA remaining in PBS (pH 7.4), GSH, and ascorbate during 12 h incubation at 37°C; each data point represents mean ± SD (n = 3); and (**B**) representative mass spectrum of sample drawn from ascorbate solution incubated OXA-OA at 12 h time point. Kinetic evaluation comprising (**C**) $\ln(C_t/C_0)$ *vs* time plot in GSH at 37°C, (**D**) $\ln(C_t/C_0)$ *vs* time plot in ascorbate at 37°C, and (**E**) reduction half-lives ($t_{1/2}$) of OXA-OA in GSH and ascorbate

models can also exhibit substantially higher basal GSH than non-tumorigenic breast epithelial cells (e.g., ~ 5 *vs* ~ 0.5 µg/mg protein in MDA-MB-231 *vs* MCF-10A) [40], which supports efficient activation in GSH-rich tumor cells. Although the rate difference was modest, it suggests that redox conditions could help shape the spatial and temporal profile of Pt(II) generation within the TME.

Design, Development and Optimization of OXA-OA Alb NPs

Preparation of OXA-OA Alb NPs

OXA-OA Alb NPs were prepared by a simple desolvation approach followed by genipin crosslinking, as previously

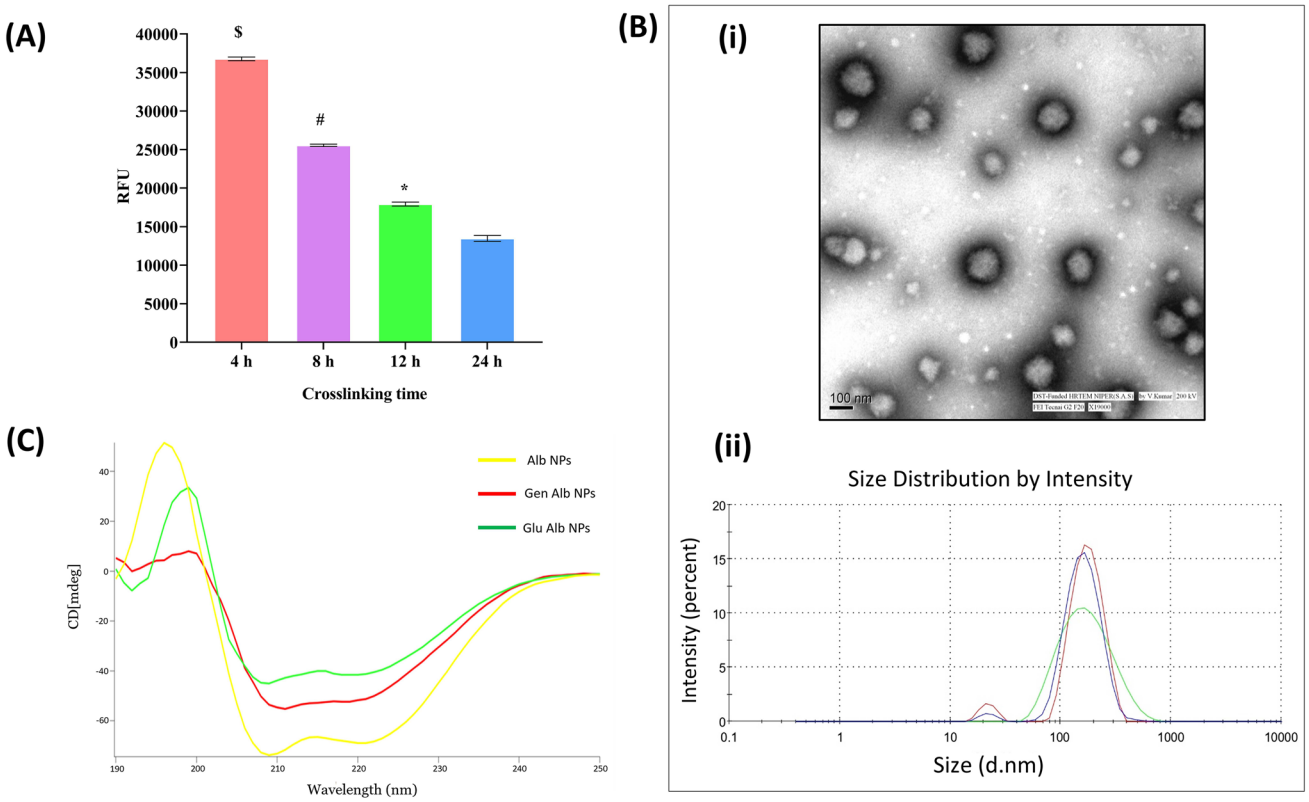

Fig. 5 Characterization of formulations: (**A**) Comparison of crosslinking times for preparing Alb NPs; each data point represents mean ± SD (n = 3); $; #; *p < 0.0001 4 h, 8 h, and 12 h *versus* 24 h. (**B**) morphological and size characterization comprising (i) TEM image of OXA-OA Alb NPs and (ii) Size distribution plot. (**C**) CD Spectra of Alb; Glu Alb NPs, Gen Alb NPs

reported [23]. To maximize matrix consolidation and drug retention, formulation variables were systematically optimized within an alkaline pH window (pH 8.5–9.0) by varying the genipin concentration, crosslinking time, and drug amount. Each condition was assessed by hydrodynamic size and size distribution, zeta potential, drug loading, entrapment efficiency (%EE), and crosslinking-associated readouts. The effects of individual parameters on NPs performance are summarized in the Supplementary file.

Crosslinking Efficiency and Time

After NPs formation, genipin crosslinking conditions were optimized to ensure structural stabilization and batch-to-batch reproducibility. Gen Alb NPs formed a stable colloidal dispersion, with a mean hydrodynamic diameter of 92.48 ± 0.25 nm and a PDI of 0.38 ± 0.01. Crosslinking progression was supported by high amino-group utilization (85.24 ± 3.87%), consistent with substantial consumption of accessible Alb primary amines and formation of a more crosslinked protein network. Mechanistically, genipin primarily reacts with primary amines via nucleophilic attack to form intra- and intermolecular linkages, and a slower pathway can involve substitution at genipin's ester functionality, contributing additional amide-type stabilization within the crosslinked matrix [41]. In line with amine consumption during crosslink formation, time-dependent fluorescence monitoring (Fig. 5A) showed a progressive decrease in the fluorescence signal associated with free primary amines, and the signal reached a plateau by 24 h under the tested conditions. Based on this endpoint, 24 h was selected as the standard crosslinking duration for all subsequent formulations.

Optimization of Genipin Concentration

After fixing the crosslinking time, we assessed how genipin concentration influenced NPs attributes and drug retention. As the genipin level increased, particle size, PDI, zeta potential, and encapsulation efficiency shifted accordingly, consistent with crosslink density-dependent tightening of the Alb network and changes in colloidal stability. The complete concentration-dependent comparison is provided in Supplementary Table S3. Based on the overall balance between dispersion stability and drug entrapment, 0.8% (w/v) genipin was selected as the optimized concentration and was used for subsequent studies.

Optimization of Drug Loading

Finally, we optimized the theoretical drug loading to maximize entrapment without compromising colloidal quality. Across the tested loading levels, NPs attributes and encapsulation efficiency changed in a loading-dependent manner (Supplementary file Table S4). Among the conditions evaluated, 7.5% drug loading provided the best overall balance between colloidal characteristics and %EE and was therefore selected as the optimized loading for downstream experiments.

Characterization of OXA-OA Alb NPs

Particle Size, Shape and Morphology Determination

The optimized OXA-OA Alb NPs formed a compact and uniform nanosuspension, with a mean hydrodynamic diameter of 140.52 ± 4.35 nm and a PDI of 0.25 ± 0.05. This degree of dispersity supports a predominantly unimodal population, which is typically considered suitable for nanoparticle systems. In practice, PDIs in the ~ 0.20–0.30 range are commonly reported and interpreted as acceptable uniformity for protein-derived colloids, whereas higher values commonly reflect broader heterogeneity and a greater likelihood of aggregation [42, 43]. For example, Das *et al*. reported Alb NPs with PDI < 0.25 and described this as confirming a uniform population, while Skoll *et al*. similarly reported PDI ≈ 0.24 for HSA nanoparticles developed for parenteral delivery. They carried a stable negative surface charge (-30.54 ± 2.04 mV) which is expected for Alb systems at near-neutral pH because Alb remains net anionic above its pI (~ 4.7) [44]. Importantly, during genipin optimization (Table S3), increasing genipin from 0.1% to 0.8% shifted zeta potential from -37.15 ± 2.35 mV to -28.15 ± 3.45 mV, suggesting that higher crosslinking density progressively moderates the apparent surface charge by consuming accessible amines and altering the charge environment at the particle-medium interface; a similar shift toward less-negative zeta potential with increasing genipin has been reported for Gen Alb NPs [45, 46]. Encapsulation efficiency remained high ($84.55 \pm 4.49\%$), confirming effective incorporation of OXA-OA within the Alb matrix. TEM and the corresponding size distribution profile (Fig. 5B(i-ii)) further confirmed predominantly spherical nanoparticles with a uniform size population.

CD Spectroscopy

To understand how crosslinking reshaped albumin's secondary structure, we compared the CD spectra of plain Alb, Glu Alb NPs, and Gen Alb NPs across 190–250 nm. Figure 5C. Plain Alb displayed the expected α-helical signature, with a positive band near ~ 193 nm and negative bands at ~ 208 and ~ 222 nm, consistent with native Alb [47]. When Alb was crosslinked with glutaraldehyde, this signature weakened substantially. The ~ 193 nm band dropped, and the minima at ~ 208 and ~ 222 nm became less pronounced, indicating partial loss of α-helical order and a more perturbed conformation. This pattern was consistent with aldehyde-driven covalent modification of lysine and other nucleophilic residues, which can constrain local packing and promote unfolding [47, 48]. In contrast, Gen Alb NPs preserved the α-helical features more closely to plain Alb even at the same crosslinker concentration (0.8% w/v). Taken together, the CD data supported genipin as the gentler crosslinker in this system, helping maintain a more native-like Alb conformation, an advantage when structural integrity is important for downstream performance.

Lyophilization Study

Freeze-drying was evaluated as a practical approach to improve the storage stability of OXA-OA Alb NPs, and post-lyophilization performance was assessed by particle size, size distribution, and reconstitution behavior in the presence of different lyoprotectants. Figure 6A. Based on our observations, most lyoprotectants showed a measurable decline in colloidal quality after freeze–thaw stress, whereas trehalose preserved the pre-lyophilization attributes more consistently. Notably, trehalose-containing samples reconstituted readily in PBS in < 1 min and yielded an intact, fluffy cake on visual inspection, suggesting minimal aggregation and good cake integrity. Figure 6A(i)&(ii). Recovery after lyophilization was quantified using the particle size ratio (S_f/S_i). An S_f/S_i value close to 1 indicates recovery toward the original dispersion, whereas $S_f/S_i > 1.5$ is typically associated with poor reconstitution [49]. In line with this criterion, 5% (w/v) trehalose yielded Sf/Si ≈ 1.25, supporting near-original size recovery after rehydration. Figure 6A(i)&(ii). Furthermore, based on preliminary experiments the concentration of trehalose was optimized within the range of 1–10% (w/v) Fig. 6A(iii)&(iv). Visual inspection showed that higher concentrations produced denser lyophilized cakes, with 5% trehalose yielding the most favorable outcome. This likely reflects the formation of a protective glassy matrix that stabilizes nanoparticles during storage and enables rapid, complete reconstitution. At this concentration, the rehydrated formulation remained uniformly suspended without visible aggregation, indicating preserved nanoparticle quality and performance.

In Vitro Release Study

To gauge how effectively the genipin-crosslinked Alb matrix moderates drug escape under physiological conditions,

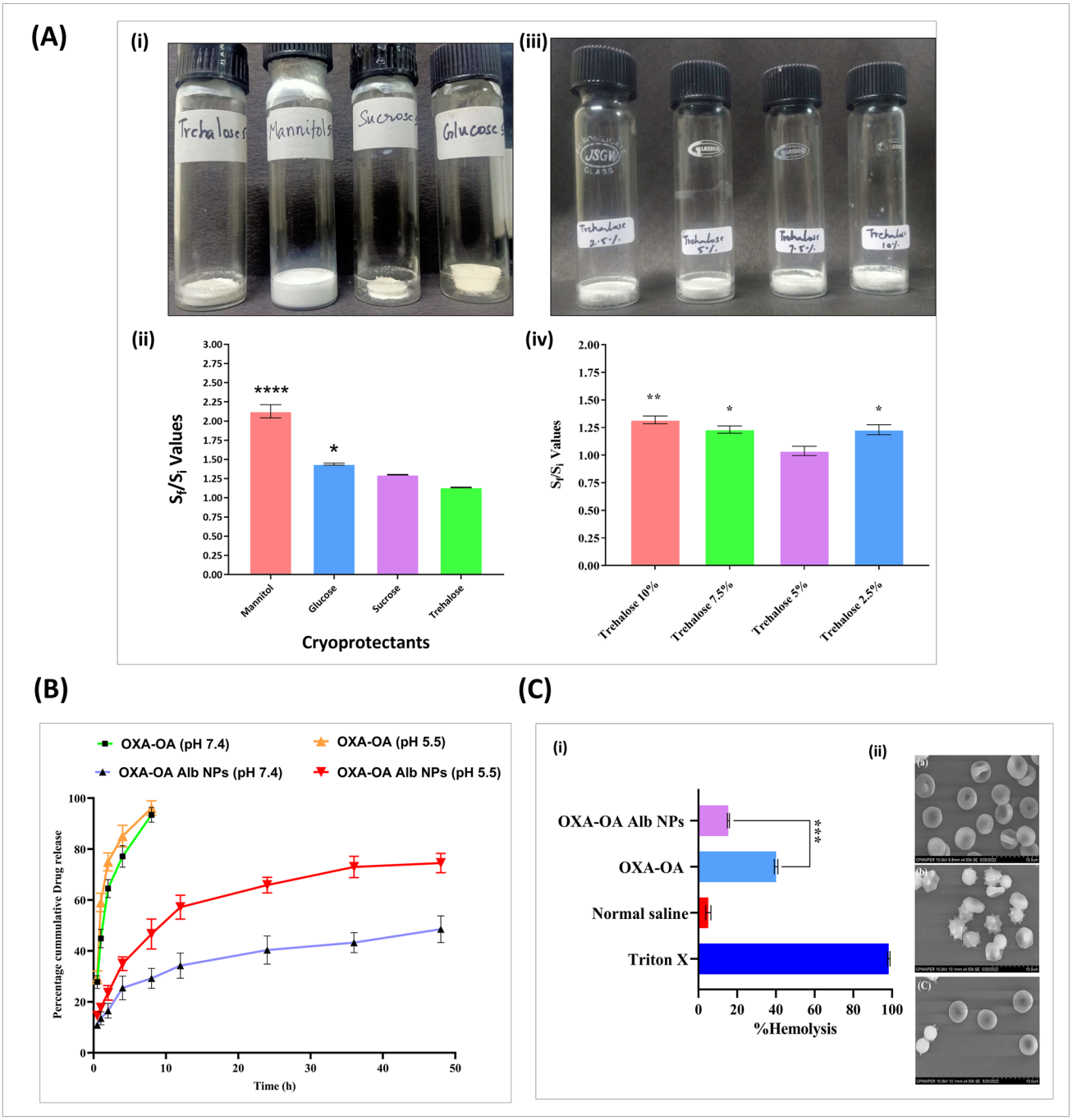

Fig. 6 Evaluation of cryoprotectant effects, drug-release behavior, and hemocompatibility of OXA-OA Alb NPs: (**A**) optimization of cryoprotectants comprising (i) lyophilized samples of NPs with different agents, (ii) S_f/S_i ratios with various cryoprotectants, (iii) lyophilized samples of NPs with various concentrations of Trehalose, and (iv) comparative S_f/S_i ratio with various concentration of trehalose. (**B**) Cumulative release profiles at pH 7.4 and pH 5.5 over 48 h. (**C**) hemocompatibility study showing (i) % hemolysis after 6 h incubation with OXA-OA, OXA-OA Alb NPs, saline, and Triton X (mean ± SD, n = 3) and (ii) SEM images of RBCs after exposure to the same treatments

we compared the diffusion of the OXA-OA conjugate in buffer with its release from the optimized OXA-OA Alb NPs. As expected in the absence of a structural scaffold, the free OXA-OA rapidly traversed the dialysis membrane, reaching ~ 93.45 ± 2.89% cumulative release by 8 h in PBS (pH 7.4, 37°C), as shown in Fig. 6B. In sharp contrast, OXA-OA Alb NPs released only ~ 29.23 ± 3.87% over the same interval and progressed slowly thereafter to ~ 48.56%

at 48 h under identical conditions. This sustained pattern points to reduced diffusivity imposed by Alb encapsulation: the protein network provides a hydrated yet sterically restrictive environment and, when crosslinked by genipin, behaves as a molecular shield that curbs premature efflux and helps stabilize the conjugate [23]. Acidic conditions further modulated release. At pH 5.5, OXA-OA Alb NPs discharged ~ 46.63% of payload by 8 h and ~ 74.50% by 48 h, consistent with pH-induced loosening of the Alb network and accelerated transport. Fitting the NP data to the Peppas-Sahlin model yielded $m \approx 0.53$, $k_1 \approx 19.5$, and $k_2 \approx -1.28$, with higher correlation ($R^2 = 0.9964$) and linearity [50], supporting diffusion-dominated kinetics ($0 < m < 1$) with a modest counteracting relaxation component, shown in Table S5. Together, these results show that genipin-crosslinked Alb nanostructures markedly temper OXA-OA diffusion at physiological pH while permitting faster payload liberation in an acidic milieu—an advantageous profile for tumor-relevant environments.

In Vitro Hemolytic Toxicity

We next examined hemocompatibility of the OXA-OA conjugate and OXA-OA Alb NPs in an RBC hemolysis assay, because membrane-active liabilities are often unmasked early when lipophilic prodrugs or amphiphile-like motifs are introduced for intravenous delivery. The % hemolysis is summarized in Fig. 6C(i). Under the tested conditions, the free conjugate produced significantly greater hemolysis compared to the formulation ($p < 0.001$), although the extent remained well below the positive control (Triton X). SEM images offered an orthogonal readout (Fig. 6C(iii)): RBCs exposed to the conjugate showed marked shape distortion with loss of the typical biconcave morphology and increased surface irregularity, supporting the quantitative hemolysis signal rather than an assay-only effect. Mechanistically, this pattern is consistent with a composition-driven membrane interaction, where the OA domain can partition into the phospholipid bilayer and promote membrane destabilization [51, 52], while the Pt center may further amplify injury through surface protein/thiol interactions that reduce membrane resilience [53]. In contrast, OXA-OA Alb NPs closely mirrored the negative control (PBS, pH 7.4) in both the hemolysis readout and SEM, with RBC morphology largely preserved and no appreciable evidence of membrane damage. Collectively, these results support that Alb encapsulation attenuated the hemolytic liability of the free conjugate, likely by shielding the hydrophobic OA functionality and limiting direct RBC contact, thereby strengthening the hemocompatibility rationale for proceeding to *in vivo* administration [54].

In Vitro Cell Line-Based Performance Evaluation

Qualitative Cellular Uptake Analysis

To visualize intracellular delivery and infer subcellular distribution of the OXA-OA, C-6 loaded NPs were prepared using the same desolvation method as a model compound. CLSM was then used to compare uptake of free C-6 *versus* NP-encapsulated C-6 in 4T1 and MDA-MB-231 cells after a 3 h incubation (Fig. 7A&B). In both cell lines, free C-6 produced only faint intracellular fluorescence, whereas NP-encapsulated C-6 yielded a markedly stronger green signal. The fluorescence from the formulation was distributed throughout the cell body with a prominent perinuclear pattern relative to DAPI staining, consistent with substantially higher intracellular accumulation than the free dye. This uptake profile is in line with how Alb-based carriers are internalized at the cellular level. Alb can engage caveolae-associated gp60-mediated transcytosis pathways and is also associated with SPARC-rich tumor phenotypes, which together can favor receptor-associated endocytosis and intracellular trafficking of Alb constructs [55–57]. Moreover, reports suggest that TNBC can adopt macropinocytic protein scavenging when nutrients are limited, which may contribute to the higher uptake observed with Alb-formulated cargo [58, 59]. This is extremely important as the localization of drug conjugate within specific cellular compartments can dramatically influence its biological efficacy [60]. By contrast, the weak signal from free C-6 was consistent with the practical limitations of delivering hydrophobic molecules, including poor solubility, rapid clearance, and potential non-specific binding [61]. Therefore, these results not only support the use of Alb NPs but also highlight the potential to improve the therapeutic index of drug conjugates when delivered in this manner.

Quantitative Cellular Uptake Analysis

Building on the imaging readout, we next quantified intracellular OXA-OA accumulation to determine whether the higher fluorescence observed with Alb-formulated cargo translated into a measurable gain in cellular delivery (Fig. 7C). In both 4T1 and MDA-MB-231 cells, OXA-OA Alb NPs showed the highest uptake at the 3 h time point, indicating that the Alb carrier increased net cellular exposure relative to the free formulations. In 4T1 cells, uptake at 3 h was 2.21-fold higher for OXA-OA Alb NPs than for free OXA and 1.07-fold higher than for free OXA-OA. A similar pattern was observed in MDA-MB-231 cells, where OXA-OA Alb NPs increased uptake by 2.13-fold *versus* OXA and 1.18-fold *versus* OXA-OA. Notably, the magnitude of improvement was larger when OXA-OA Alb NPs were compared with free OXA than with the free OXA-OA,

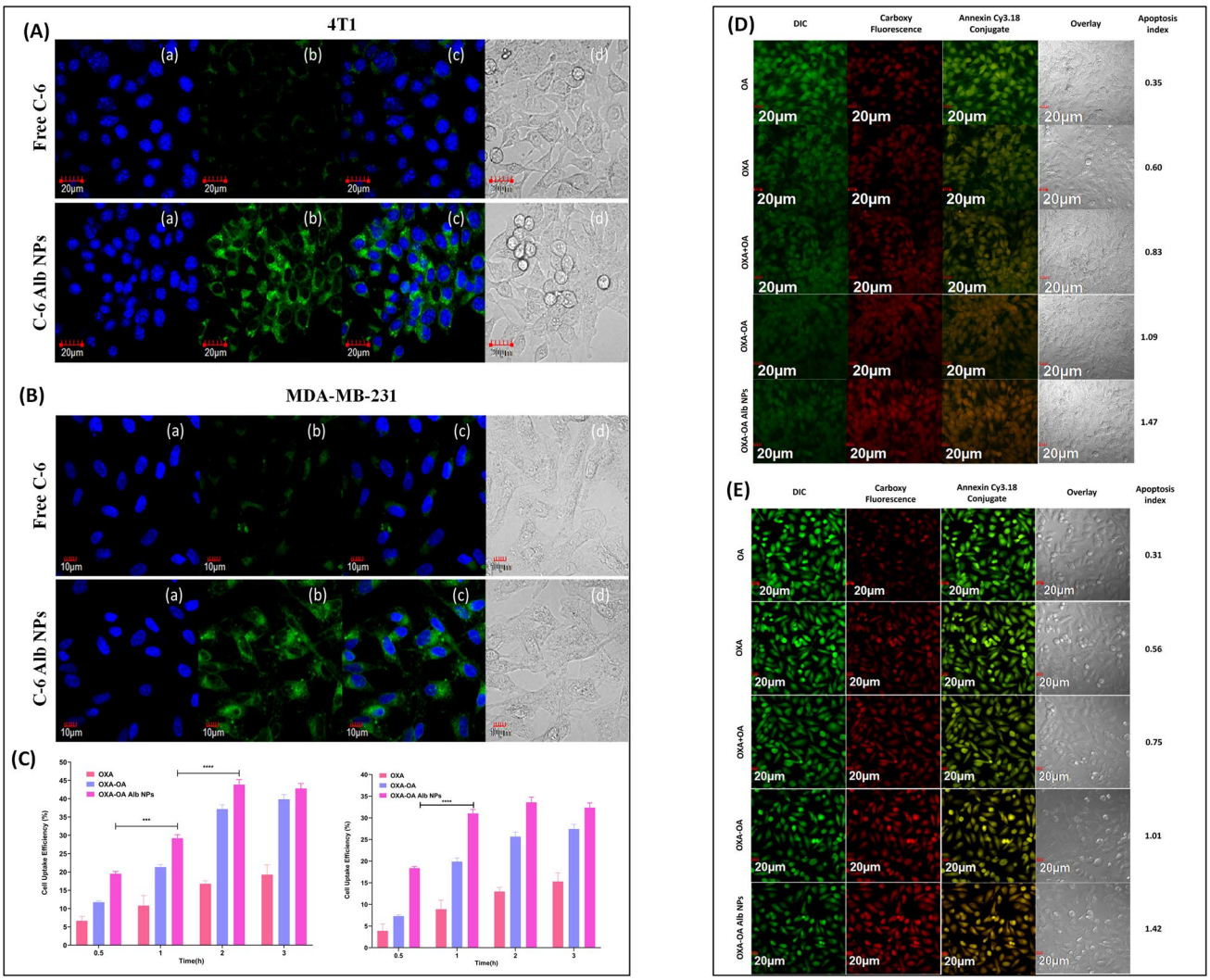

Fig. 7 Evaluation of cellular uptake, cytotoxicity, and apoptosis induction of formulation: CLSM images of (**A**) 4T1 (**B**) MDA MB-231 cell lines treated with free C-6 and C-6 Alb NPs. In all images; (a) DAPI is used as counterstain, (b) green fluorescence channel, (c) superimposition of (a) and (b), and (d) differential interface contrast images; (**C**) Quantitative cell uptake study in 4T1 (left panel) and MDA-MB-231 (right panel) cell line; each data point represents mean ± SD (n = 3). Apoptosis evaluation comprising (**D**) 4T1 and (**E**) MDA-MB-231; panels shown as DIC, green channel, annexin (red), conjugate/overlay, and apoptosis index

suggesting that the carrier primarily enhanced cell association and internalization efficiency rather than simply increasing the intrinsic membrane affinity of the OA-modified drug [62]. This quantitative hierarchy also supports a practical interpretation for the weaker performance of free OXA-OA, where protein sequestration in biological media and the need for intracellular activation of the Pt(IV) conjugate can reduce the fraction that reaches intracellular targets [63].

In Vitro Cell Cytotoxicity Assay

In vitro cytotoxicity assessment revealed a clear, concentration-dependent reduction in cell viability in 4T1 and MDA-MB-231 cells treated with OXA, OA, OXA-OA, or OXA-OA Alb NPs. Across the full concentration range, OXA-OA Alb NPs consistently produced the greatest loss of viability, translating into the lowest IC_{50} values in both models (0.19 ± 0.36 µg/mL in 4T1 and 0.20 ± 0.16 µg/mL in MDA-MB-231). Relative to the free OXA-OA combination, these IC_{50} values represented ~ 3.73-fold (4T1) and 4.20-fold (MDA-MB-231) greater potency [62, 63]. The advantage was even more pronounced *versus* the single components, with ~ 25- and 30-fold lower IC_{50} values compared with free OXA and ~ 50- and 58-fold lower IC_{50} values compared with free OA, respectively [64, 65]. Notably, the formulation also outperformed the physical mixture (OXA + OA) by > ten-fold in both cell lines, indicating that co-delivery in an Alb matrix provided more than simple additivity (Table I). This

potency hierarchy was consistent with two converging considerations. First, Alb-based carriers have been reported to enhance intracellular exposure by reducing effective drug efflux and improving productive internalization [66]. Second, OA has also been reported to sensitize tumor cells to cytotoxic therapy in combination settings (e.g., with taxol), supporting a functional contribution when OA is co-delivered at the cellular level [67]. In our system, the enhanced cytotoxicity could plausibly reflect intracellular activation of the OXA(IV) conjugate with regeneration of OXA(II) alongside OA, thereby favoring concurrent exposure to both components and a cooperative cytotoxic response.

Annexin V Apoptosis Assay

The apoptosis effects of previously mentioned compounds were evaluated in the 4T1 (Fig. 7D) and MDA-MB-231 (Fig. 7E) cell lines and revealed substantial outcomes. Cells treated with OA showed apoptosis indices of 0.35 (4T1) and 0.31 (MDA-MB-231), consistent with a modest pro-apoptotic effect. In contrast, OXA showed higher apoptosis indices (0.60 and 0.56, respectively), consistent with its known ability to engage cell-death pathways in cancer cells. OXA-OA further increased the apoptosis index to 0.83 (4T1) and 0.75 (MDA-MB-231), which was consistent with improved cellular association of the more lipophilic conjugate [63]. To benchmark simple co-administration, the physical mixture (OXA + OA) yielded indices of 1.09 (4T1) and 1.01 (MDA-MB-231), supporting enhanced apoptosis relative to either component alone. Because Pt(IV) prodrugs are typically activated by intracellular reduction in GSH-rich environments, the higher activity of OXA-OA was also consistent with more efficient intracellular conversion to the active platinum species following uptake. In addition, OA has been reported to augment FASN expression in TNBC, which may further shape the lipid-metabolic context relevant to OA-bearing constructs [68]. The apoptosis effect, however, was most pronounced in cells treated with OXA-OA Alb NPs, which displayed an apoptosis index of 1.47 (4T1) and 1.42 (MDA-MB-231), the highest among all the examined groups. The index was approximately 4.19 and 2.43-fold (4T1); 4.50- and 2.53-fold (MDA-MB-231) greater than that produced by OA and OXA individually, and roughly 1.32 and 1.26-fold greater than that of the free OXA-OA respectively. Although absolute indices were higher in 4T1, the relative gain with Alb NPs was greater in MDA-MB-231. It appears that the amplification in apoptosis was achieved through the targeted delivery of Alb NPs to tumor cells, which improved cellular uptake and conjugate delivery, as shown qualitatively. Moreover, encapsulating OXA-OA into Alb NPs likely enhanced its bioavailability and stability. Overall, the apoptosis profile aligned with the uptake findings and supported enhanced cytotoxic efficacy of OXA-OA Alb NPs in TNBC cells.

In Vivo Antitumor Activity

The *in vivo* antitumor efficacy was evaluated in a 4T1 orthotopic BALB/c model following a reported protocol [69]. Across readouts, OXA-OA Alb NPs produced the most pronounced tumor growth control relative to free OXA and the OXA-OA conjugate. As illustrated in Fig. 8A, tumors in the control group expanded rapidly and reached ~ 2,000 mm^3 by day 20. In contrast, the group treated with OXA-OA Alb NPs maintained tumor volumes below ~ 400 mm^3 over the same period, indicating substantially stronger growth suppression than OXA alone. Quantitatively, tumor size was reduced 5.89-fold *versus* free OXA and 2.16-fold *versus* the OXA-OA conjugate, consistent with improved therapeutic performance of the final formulation. This pattern was reinforced by tumor inhibition rates (Fig. 8B): OXA-OA Alb NPs achieved ~ 90% inhibition, compared with ~ 40% for OXA and ~ 78% for OXA-OA. The higher inhibition rate observed with OXA-OA Alb NPs was consistent with improved tumor delivery by the Alb NPs platform and reduced premature loss of the OXA-OA prodrug, supporting sustained intratumoral exposure and controlled release. Alb can enhance cellular uptake through receptor-mediated endocytosis, including pathways involving gp60 and SPARC (secreted protein acidic and rich in cysteine), which are reported to be overexpressed in TNBC [48], thereby favoring tumor accumulation. Consistent with the tumor-volume findings, OXA-OA Alb NPs produced the greatest reductions in tumor weight and burden, achieving up to ~ 80% reduction *versus* the untreated control group (Fig. 8C&D). The excised tumor images further supported these quantitative results, with substantially smaller tumors in the OXA-OA Alb NP group than in the other groups (Fig. 8E). The differences between treatment groups were statistically significant, supporting the improved antitumor efficacy of OXA-OA Alb NPs in this model and warranting follow-up studies to assess post-treatment recurrence and metastatic burden.

Table I IC_{50} Values based on MTT Assay; All the Values are Represented as Mean ± SD ($n = 3$)

Formulation	IC_{50} values (μg/mL)	
	4T1	MDA-MB-231
Free OA	10.18 ± 0.84	12.01 ± 0.55
Free OXA	4.86 ± 0.56	6.06 ± 0.68
Free OXA + OA	2.26 ± 0.48	3.51 ± 0.89
Free OXA-OA conjugate	0.71 ± 0.98	0.84 ± 0.14
OXA-OA Alb NPs	0.19 ± 0.36	0.20 ± 0.16

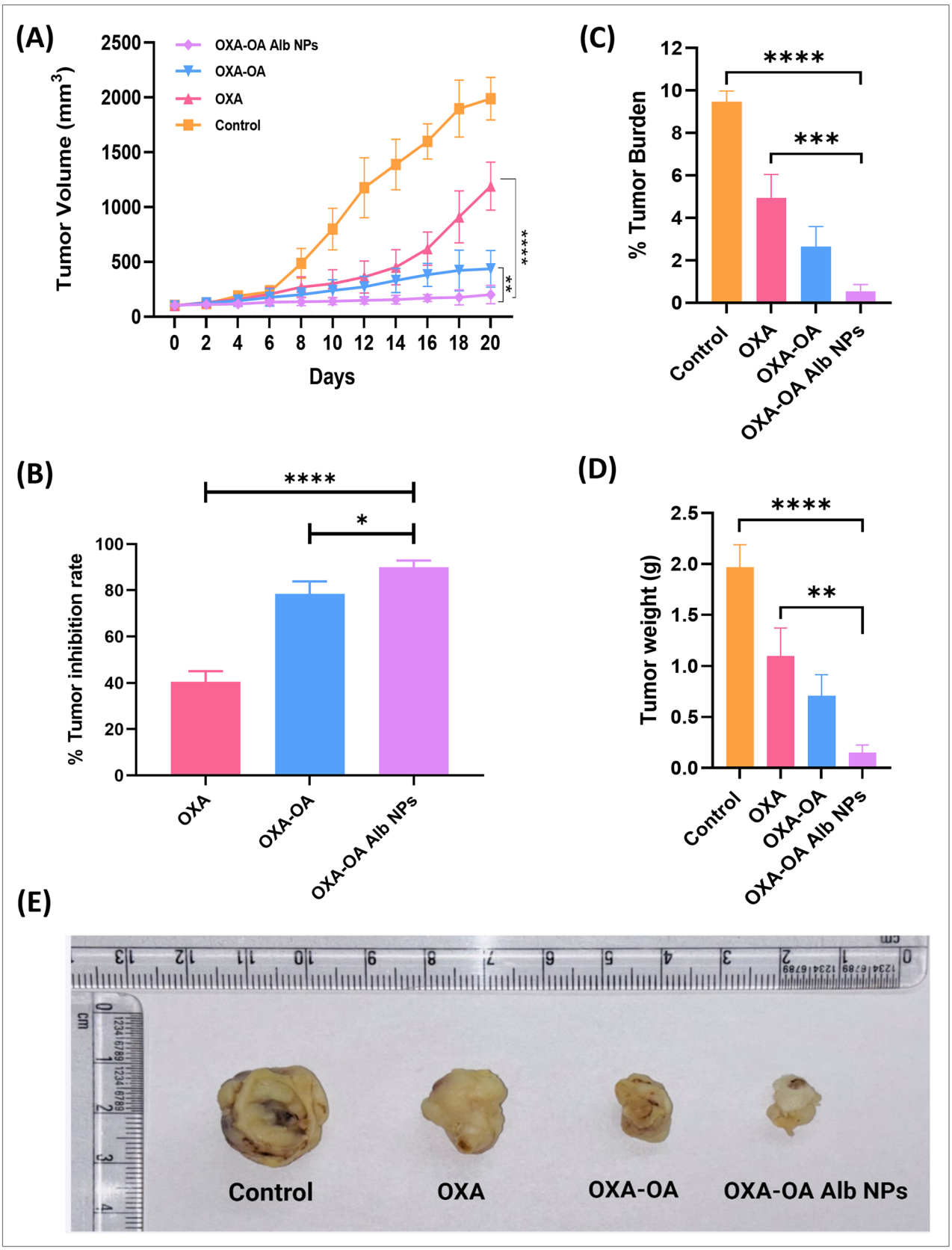

◂**Fig. 8** Illustrates anticancer study performed in 4T1 induced BALB/c mice model: The antitumor efficacy was evaluated in terms of (**A**) tumor volume reduction (mm^3), (**B**) tumor inhibition rate (%), (**C**) tumor burden (%), (**D**) tumor weight (g), (**E**) visual representation of the tumor size variation, displays a digital photograph of the excised tumors from different treatment group, presented with a ruler for scale; each data point represents mean ± SD (n = 3); where * = P < 0.05; ** = P < 0.01; *** = P < 0.001; **** = P < 0.0001; ns = P > 0.05 compared to control

Toxicity Study

We determined the systemic toxicity of OXA, OXA-OA, and OXA-OA Alb NPs by profiling serum liver and kidney biomarkers and by examining histological changes in major organs. Liver injury markers, ALT (Fig. 9A) and AST (Fig. 9B) showed no significant differences among the control, OXA, OXA-OA, and OXA-OA Alb NP groups (P > 0.05), indicating no evident hepatotoxicity across treatments under the tested regimen. By contrast, renal function indices displayed a clearer treatment-dependent trend. Both BUN (Fig. 9C) and creatinine (Fig. 9D) were elevated in the free OXA group relative to the control [70]. OXA-OA and OXA-OA Alb NPs showed a reduction toward baseline, suggesting a potential nephroprotective effect of the conjugate and nanoformulation. Histopathological analysis further corroborated these biochemical findings. Figure 9E. Animals treated with OXA exhibited mild-to-moderate structural alterations in the kidney and additional signs of organ stress in the heart, spleen, liver, and lung. By comparison, OXA-OA and especially OXA-OA Alb NPs showed less pronounced changes, with tissue architecture in the OXA-OA Alb NP group appearing close to the control. Collectively, the combined biomarker and histology readouts support a reduced off-target organ injury profile after prodrug modification and Alb encapsulation, with the strongest improvement observed for OXA-OA Alb NPs.

Conclusion

In summary, this study positions lipid-metallodrug conjugation coupled with protein nanoencapsulation as a strategy to overcome key barriers in treating TNBC, an aggressive breast cancer subtype with limited targeted options. We designed the OXA-OA conjugate and formulated it within Alb NPs to address major therapeutic constraints associated with free OXA, including systemic toxicity, suboptimal bioavailability, and inadequate tumor-selective delivery. OXA-OA significantly enhanced apoptosis and cytotoxicity in tumor cells. This effect is plausibly enabled by GSH-mediated OXA(IV) reduction. It is also consistent with complementary contributions from OXA-driven DNA damage and OA-linked pro-apoptotic effects. Alb NPs encapsulation further improved therapeutic performance by promoting tumor accumulation via the EPR effect and facilitating receptor-mediated endocytosis, thereby increasing intratumoral delivery and retention. The optimized OXA-OA Alb NPs provided controlled release, achieved marked tumor growth inhibition *in vivo*, and improved tolerability relative to free OXA, as reflected by preserved liver and kidney biomarkers and minimal histopathological injury in major organs. Collectively, these results support a dual-functional platform that integrates lipid-drug conjugates with nanotechnology-enabled delivery to enhance antitumor activity; however, lack of *in vivo* PK data remains a key limitation. Based on its preliminary performance, this platform can be explored in aggressive, lipid-enriched cancers, including to determine whether it can also suppress metastasis, while assessing durability and compatibility with immunotherapy/checkpoint blockade. Overall, OXA-OA Alb NPs represent a robust and adaptable framework for advancing metallotherapeutic conjugates toward safer and more effective treatment paradigms across aggressive malignancies.

Abbreviations *^1H NMR*: Proton Nuclear Magnetic Resonance; *^{13}C NMR*: Carbon-13 Nuclear Magnetic Resonance; *Alb*: Albumin; *AKT*: Protein kinase B; *ALT*: Alanine Aminotransferase; *AP-1*: Activator Protein-1; *AST*: Aspartate Aminotransferase; *Alb NPs*: Albumin Nanoparticles; *BALB/c*: Bagg Albino laboratory mouse, substrain C; *BRCA1/2*: Breast Cancer gene 1/2; *BCRF*: Breast Cancer Research Foundation; *BUN*: Blood Urea Nitrogen; *C-6*: Coumarin-6 (fluorescent dye); *CD*: Circular Dichroism; *CLSM*: Confocal Laser Scanning Microscopy; *DAPI*: 4′,6-Diamidino-2-phenylindole; *DMF*: Dimethylformamide; *DMSO*: Dimethyl Sulfoxide; *DPBS*: Dulbecco's Phosphate Buffered Saline; *EPR*: Enhanced Permeability and Retention; *EGFR*: Epidermal Growth Factor Receptor; *ER*: Estrogen receptor; *ERK*: Extracellular signal-regulated kinase; *ESI*: Electrospray ionization; *%EE*: Percent encapsulation efficiency; *FAK*: Focal adhesion kinase; *FASN*: Fatty Acid Synthase; *FDA*: Food and Drug Administration; *FITC*: Fluorescein Isothiocyanate; *FTIR*: Fourier-Transform Infrared spectroscopy; *GSH*: Glutathione; *gp60*: 60-KDa glycoprotein; *H&E*: Hematoxylin and eosin (histology stain); *HER2*: Human Epidermal Growth Factor Receptor 2; *HPLC*: High-Performance Liquid Chromatography; *HRMS*: High-Resolution Mass Spectrometry; *IC_{50}*: Half Maximal Inhibitory Concentration; *MTT*: 3-(4,5-Dimethylthiazol-2-yl)-2,5-diphenyltetrazolium bromide; *MWCO*: Molecular Weight Cut-Off; *NPs*: Nanoparticles; *OA*: Oleic Acid; *OXA*: Oxaliplatin; *PBS*: Phosphate Buffered Saline; *PDI*: Polydispersity Index; *PTEN*: Phosphatase and tensin homolog; *RBC*: Red blood cell; *RFU*: Relative Fluorescent Units; *SEM*: Scanning Electron Microscopy; *SPARC*: Secreted Protein Acidic and Rich in Cysteine; *TEM*: Transmission electron microscope; *TIR*: Tumor inhibition rate; *TME*: Tumor microenvironment; *TNBC*: Triple-Negative Breast Cancer; *UV-Vis*: Ultraviolet-visible

Supplementary Information The online version contains supplementary material available at https://doi.org/10.1208/s12249-026-03353-2.

Acknowledgements The authors would like to acknowledge the Director, NIPER S.A.S. Nagar for providing the necessary facilities and infrastructure. Technical assistance provided by Mr. Rahul Mahajan is also duly acknowledged.

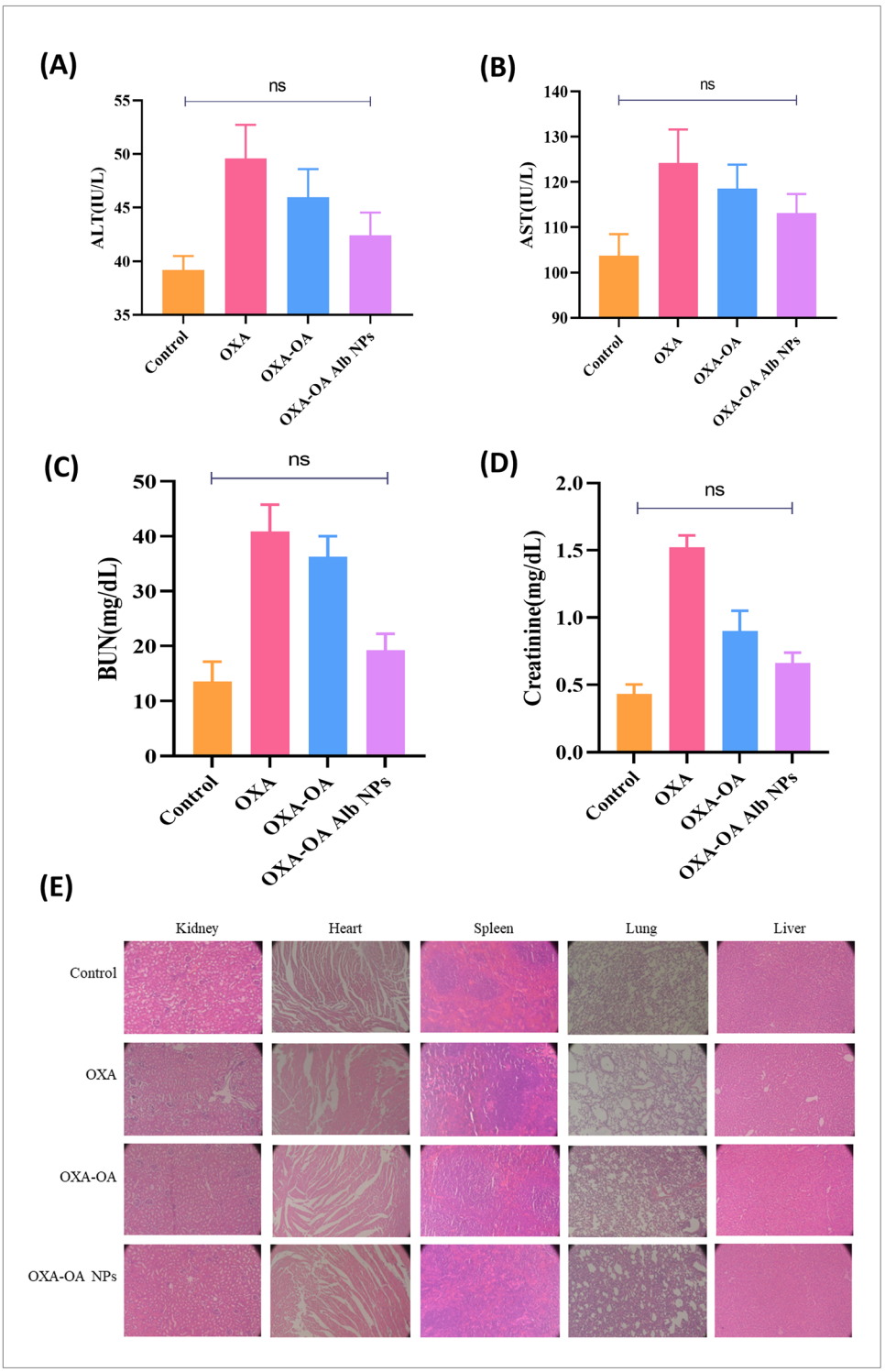

Fig. 9 *In vivo* toxicity evaluation of different treatment group: Biochemical and histopathological evaluation of systemic toxicity, comprising (**A**) ALT, (**B**) AST, (**C**) BUN, and (**D**) creatinine levels across different treatment groups; (**E**) Representative histopathological assessment of organ toxicity, displaying microscopic images (20X magnification) of H&E-stained sections from kidney, heart, spleen, lung, and liver tissues of treated mice

Author Contributions Oly katari: Conceptualization, execution, methodology, investigation, validation, data curation, visualization, writing-original draft. S. Lokesh: Execution, analysis, methodology, investigation, data curation, interpretation and validation. Brojendra Nath Saren: Analysis, data curation, interpretation, data validation, Formal analysis Software/Statistical analysis, writing-draft, review & editing. Vivek Yadav: Conceptualization, methodology, visualization, contribution in cell culture and animal studies. Kaushik Kuche: Conceptualization, validation, contribution in cell culture and animal studies. Sanyog Jain: Resources, funding acquisition, supervision, project administration, writing-review & editing.

Funding The authors are thankful to the Science and Engineering Research Board (ASEAN-SERB), the Department of Science and

Technology (DST), Ministry of Science and Technology, Government of India for financial assistance.

Data Availability The authors confirm that the data for this study findings are available within the article and the supplementary information file.

Declarations

Conflict of interest The authors declare that they have no competing financial or personal relationships that could have influenced the work reported in this manuscript.

References

1. Torrisi R, Gerosa R, Miggiano C, Saltalamacchia G, Benvenuti C, Santoro A. Beyond failure of endocrine-based therapies in HR+/HER2 negative advanced breast cancer: what before chemotherapy? A glimpse into the future. Crit Rev Oncol Hematol. 2025;1(208):104634.
2. Debnath A, Mazumder R. Clinical progress of targeted therapy for breast cancer: a comprehensive review. Curr Cancer Drug Targets. 2025J;25(6):555–73.
3. Chen Y, Salas LA, Marotti JD, Jenkins NP, Cheng C, Miller TW, et al. Extensive epigenomic dysregulation is a hallmark of homologous recombination deficiency in triple-negative breast cancer. Int J Cancer. 2025;156(6):1191–202.
4. Takashima A, Hamaguchi T, Mizusawa J, Nagashima F, Ando M, Ojima H, et al. Oxaliplatin Added to Fluoropyrimidine/Bevacizumab as Initial Therapy for Unresectable Metastatic Colorectal Cancer in Older Patients: A Multicenter, Randomized, Open-Label Phase III Trial (JCOG1018). J Clin Oncol. 2024Nov 20;42(33):3967–76.
5. Li S, Li T, Wang X, Rahmatulla A, Zhao Y, Zhang X, et al. Research progress of treating ulcerative colitis and colon cancer by using oral colon targeted drug delivery system based on polymer micelles. J Drug Target. 2025Oct 21;33(9):1529–54.
6. Gebremedhn EG, Shortland PJ, Mahns DA. The incidence of acute oxaliplatin-induced neuropathy and its impact on treatment in the first cycle: a systematic review. BMC Cancer. 2018Apr 12;18(1):410.
7. Zheng YR, Suntharalingam K, Johnstone TC, Yoo H, Lin W, Brooks JG, et al. Pt(IV) prodrugs designed to bind non-covalently to human serum albumin for drug delivery. J Am Chem Soc. 2014Jun 18;136(24):8790–8.
8. Ratzon E, Najajreh Y, Salem R, Khamaisie H, Ruthardt M, Mahajna J. Platinum (IV)-fatty acid conjugates overcome inherently and acquired Cisplatin resistant cancer cell lines: an in-vitro study. BMC Cancer. 2016Feb 23;16(1):140.
9. Kim JS, Kim DK, Moon JY, Lee MY, Cho SK. Oleic acid inhibits the migration and invasion of breast cancer cells with stemness characteristics through oxidative stress-mediated attenuation of the FAK/AKT/NF-κB pathway. J Funct Foods. 2024May;1(116):106224.
10. Wardana TAP, Nuringtyas TR, Wijayanti N, Hidayati L. Phytochemical analysis of agarwood (Gyrinops versteegii (Gilg.) Domke) leaves extracts as anticancer using GC-MS. AIP Conf Proc. 2019 Dec 18;2194(1):020136.
11. Guo Z, Bergeron KF, Mounier C. Oleate promotes triple-negative breast cancer cell migration by enhancing filopodia formation through a PLD/Cdc42-dependent pathway. Int J Mol Sci. 2024;25(7):3956.
12. Yang K, Wang X, Song C, He Z, Wang R, Xu Y, et al. The role of lipid metabolic reprogramming in tumor microenvironment. Theranostics. 2023Mar 13;13(6):1774–808.
13. Guo Z, Li Y, Guo Y, Zhang A, Huo X, Song Y, et al. Oleic acid activates TGFβ-Smad3 signaling to promote ovarian cancer progression. J Ovarian Res. 2025Aug 11;18(1):180.
14. Huber AH, Kleinfeld AM. Unbound free fatty acid profiles in human plasma and the unexpected absence of unbound palmitoleate. J Lipid Res. 2017;58(3):578–85.
15. Mann J, Reznik E, Santer M, Fongheiser MA, Smith N, Hirschhorn T, et al. Ferroptosis inhibition by oleic acid mitigates iron-overload-induced injury. Cell Chem Biol. 2024Feb 15;31(2):249-264.e7.
16. Li C, Zhang D, Pan Y, Chen B. Human serum albumin based nanodrug delivery systems: recent advances and future perspective. Polymers. 2023A;15(16):3354.
17. Ji Q, Zhu H, Qin Y, Zhang R, Wang L, Zhang E, et al. GP60 and SPARC as albumin receptors: key targeted sites for the delivery of antitumor drugs. Front Pharmacol. 2024Jan;23(15):1329636.
18. Cho H, Jeon SI, Ahn CH, Shim MK, Kim K. Emerging albumin-binding anticancer drugs for tumor-targeted drug delivery: current understandings and clinical translation. Pharmaceutics. 2022M;14(4):728.
19. Schueffl H, Theiner S, Hermann G, Mayr J, Fronik P, Groza D, et al. Albumin-targeting of an oxaliplatin-releasing platinum(IV) prodrug results in pronounced anticancer activity due to endocytotic drug uptake in vivo. Chem Sci. 2021Oct 6;12(38):12587–99.
20. Li H, Quan J, Zhang M, Yung BC, Cheng X, Liu Y, et al. Lipid-Albumin Nanoparticles (LAN) for Therapeutic Delivery of Antisense Oligonucleotide against HIF-1α. Mol Pharm. 2016Jul 5;13(7):2555–62.
21. Li H, Liu Y, Chen L, Liu Q, Qi S, Cheng X, et al. Folate receptor-targeted lipid-albumin nanoparticles (F-LAN) for therapeutic delivery of an Akt1 antisense oligonucleotide. J Drug Target. 2018;26(5–6):466–73.
22. Date T, Kuche K, Chaudhari D, Ghadi R, Sahel DK, Chitkara D, et al. Hitting multiple cellular targets in triple-negative breast cancer using dual-action Cisplatin(IV) prodrugs for safer synergistic chemotherapy. ACS Biomater Sci Eng. 2022J;8(6):2349–62.
23. Abhang K, Dighe S, Katari O, Yadav V, Jain S. Dual acting oxaliplatin (IV) prodrug loaded albumin nanoparticles for safer synergistic anticancer action against triple negative breast cancer. Drug Deliv Transl Res. 2025 Dec 1;15(12):4550–70.
24. Date T, Kuche K, Ghadi R, Kumar P, Jain S. Understanding the Role of Axial Ligands in Modulating the Biopharmaceutical Outcomes of Cisplatin(IV) Derivatives. Mol Pharm. 2022May 2;19(5):1325–37.
25. Jain AK, Thanki K, Jain S. Co-encapsulation of tamoxifen and quercetin in polymeric nanoparticles: implications on oral bioavailability, antitumor efficacy, and drug-induced toxicity. Mol Pharm. 2013Sep 3;10(9):3459–74.
26. Kushwah V, Agrawal AK, Dora CP, Mallinson D, Lamprou DA, Gupta RC, et al. Novel gemcitabine conjugated albumin nanoparticles: a potential strategy to enhance drug efficacy in pancreatic cancer treatment. Pharm Res. 2017;34(11):2295–311.
27. Sharma S, Parveen R, Chatterji BP. Toxicology of nanoparticles in drug delivery. Curr Pathobiol Rep. 2021;9(4):133–44.
28. Kuche K, Yadav V, Dharshini M, Ghadi R, Chaudhari D, Date T, et al. Synergistic anticancer therapy via ferroptosis using modified bovine serum albumin nanoparticles loaded with sorafenib and simvastatin. Int J Biol Macromol. 2023Dec 31;253(Pt 8):127254.
29. Ghadi R, Pandey PK, Gabhale A, Wadikar A, Dharshini M, Kuche K, et al. Genipin-crosslinked albumin nanoparticles containing neratinib and silibinin: A dual-death therapy for triple negative breast cancer. Int J Pharm. 2023Dec;15(648):123570.

30. Chaudhari D, Katari O, Ghadi R, Kuche K, Date T, Bhargavi N, et al. Unfolding the potency of adenosine in targeting triple negative breast cancer via paclitaxel-incorporated pH-responsive stealth liposomes. ACS Biomater Sci Eng. 2022A;8(8):3473–84.
31. Kuche K, Yadav V, Dharshini M, Ghadi R, Chaudhari D, Date T, et al. Synergistic anticancer therapy *via* ferroptosis using modified bovine serum albumin nanoparticles loaded with sorafenib and simvastatin. Int J Biol Macromol. 2023Dec;31(253):127254.
32. Niu S, Zhou Y, Yu H, Lu C, Han K. Investigation on thermal degradation properties of oleic acid and its methyl and ethyl esters through TG-FTIR. Energy Convers Manag. 2017Oct;1(149):495–504.
33. Reis TA, Matos BN, Lima EM, Chaker JA, Gratieri T, Cunha-Filho MSS, et al. Oxaliplatin preformulation studies for the development of innovative topical drug delivery systems. J Therm Anal Calorim. 2017;130(3):1671–81.
34. Chen S, Zhou Q, Ng KY, Xu Z, Xu W, Zhu G. Advances in technical strategies for monitoring the reduction of platinum(iv) complexes. Inorg Chem Front. 2024;11(11):3085–118.
35. Andrés CMC, Pérez de la Lastra JM, Bustamante Munguira E, Andrés Juan C, Pérez-Lebeña E. Anticancer Activity of Metallodrugs and Metallizing Host Defense Peptides—Current Developments in Structure-Activity Relationship. Int J Mol Sci. 2024 Jul 3;25(13):7314.
36. Kastner A, Mendrina T, Bachmann F, Berger W, Keppler BK, Heffeter P, et al. Tumor-targeted dual-action NSAID-platinum(iv) anticancer prodrugs. Inorg Chem Front. 2023;10(14):4126–38.
37. P. Varbanov H, Ortiz D, Höfer D, Menin L, S. Galanski M, K. Keppler B, et al. Oxaliplatin reacts with DMSO only in the presence of water. Dalton Trans. 2017;46(28):8929–32.
38. Fronik P, Gutmann M, Vician P, Stojanovic M, Kastner A, Heffeter P, et al. A platinum(IV) prodrug strategy to overcome glutathione-based oxaliplatin resistance. Commun Chem. 2022Apr 6;5(1):1–13.
39. B. Mobley E, Byrd N, G. Yim M, Gariepy R, Rieder M, Ward S. Glutathione sensitive vesicles prepared from supramolecular amphiphiles. Soft Matter. 2021;17(42):9664–9.
40. Zhu Y, Yue P, Dickinson CF, Yang JK, Datanagan K, Zhai N, et al. Natural product preferentially targets redox and metabolic adaptations and aberrantly active STAT3 to inhibit breast tumor growth in vivo. Cell Death Dis. 2022Dec 6;13(12):1022.
41. Conghaile PÓ, Kumar R, Ferrer ML, Leech D. Glucose oxidation by enzyme electrodes using genipin to crosslink chitosan, glucose oxidase and amine-containing osmium redox complexes. Electrochem Commun. 2020;1(113):106703.
42. Huang H, Liu Q, Zhang T, Zhang J, Zhou J, Jing X, et al. Farnesylthiosalicylic Acid-Loaded Albumin Nanoparticle Alleviates Renal Fibrosis by Inhibiting Ras/Raf1/p38 Signaling Pathway. Int J Nanomedicine. 2021;16:6441–53.
43. Skoll K, Palmetzhofer J, Lummerstorfer M, Anzengruber M, Gabor F, Wirth M. Human serum albumin nanoparticles as a versatile vehicle for targeted delivery of antibiotics to combat bacterial infections. Nanomedicine Nanotechnol Biol Med. 2023;1(50):102685.
44. Mathur A, Blais S, Goparaju CMV, Neubert T, Pass H, Levon K. Development of a biosensor for detection of pleural mesothelioma cancer biomarker using surface imprinting. PLoS One. 2013M;8(3):e57681.
45. Kurtul ED, Yurtsever MÇ. Genipin Crosslinked Human Serum Albumin Nanoparticles. Bitlis Eren Üniversitesi Fen Bilim Derg. 2022Jun 30;11(2):613–9.
46. Luo R, Lin M, Zhang C, Shi J, Zhang S, Chen Q, et al. Genipin-crosslinked human serum albumin coating using a tannic acid layer for enhanced oral administration of curcumin in the treatment of ulcerative colitis. Food Chem. 2020Nov;15(330):127241.
47. Paul S, Sepay N, Sarkar S, Roy P, Dasgupta S, Sardar P, et al. Interaction of Serum Albumins with Fluorescent Ligand 4-Azido Coumarin: Spectroscopic Analysis and Molecular Docking Studies. New J Chem. 2017Nov;3:41.
48. Ghadi R, Pandey PK, Gabhale A, Wadikar A, Dharshini M, Kuche K, et al. Genipin-crosslinked albumin nanoparticles containing neratinib and silibinin: A dual-death therapy for triple negative breast cancer. Int J Pharm. 2023Dec;15(648):123570.
49. Wang Y, Kho K, Cheow WS, Hadinoto K. A comparison between spray drying and spray freeze drying for dry powder inhaler formulation of drug-loaded lipid-polymer hybrid nanoparticles. Int J Pharm. 2012Mar 15;424(1–2):98–106.
50. Iqbal H, Razzaq A, Yuan Z, Zhai L, Wang Y, Ur-Rehman U, et al. Albumin Nanocages with Methotrexate and Chondroitin Sulfate as a Dual pH/GSH-Responsive Tumor Targeting Nanomedicine for Synergistic Cancer Therapy. Biomater Res. 2025Sep;3(29):0245.
51. Wennberg C, Lundborg M, Lindahl E, Norlén L. Understanding Drug Skin Permeation Enhancers Using Molecular Dynamics Simulations. J Chem Inf Model. 2023Jul 18;63(15):4900–11.
52. Yadav R, Adikessavane N, Ram Mahato R, Maiti S. Decoding information entropy of fatty acid and phospholipid vesicles via ordering combinatorial output of hydrazones. Chem Sci. 2025;16(37):17184–92.
53. Wang J, Tao J, Jia S, Wang M, Jiang H, Du Z. The protein-binding behavior of platinum anticancer drugs in blood revealed by mass spectrometry. Pharmaceuticals. 2021;14(2):104.
54. Elblbesy MA. Hemocompatibility of Albumin Nanoparticles as a Drug Delivery System—An in Vitro Study. J Biomater Nanobiotechnology. 2016Mar 31;7(2):64–71.
55. Jiang Q, Yao F, An Y, Lai X, Li X, Yu Z, et al. Novel nanotherapeutics for cancer immunotherapy by albumin nanoparticles functionalized with PD-1 and PD-L1 aptamers. Cancer Nanotechnol. 2024Jan 6;15(1):3.
56. Kunde SS, Wairkar S. Targeted delivery of albumin nanoparticles for breast cancer: a review. Colloids Surf B Biointerfaces. 2022;1(213):112422.
57. Kummitha CM, Malamas AS, Lu ZR. Albumin pre-coating enhances intracellular siRNA delivery of multifunctional amphiphile/siRNA nanoparticles. Int J Nanomedicine. 2012;2(7):5205–14.
58. Xu G, Zhang Q, Cheng R, Qu J, Li W. Survival strategies of cancer cells: the role of macropinocytosis in nutrient acquisition, metabolic reprogramming, and therapeutic targeting. Autophagy. 2025;21(4):693–718.
59. Stukan I, Żuk A, Pukacka K, Mierzejewska J, Pawłowski J, Kowalski B, et al. Wolf in Sheep’s Clothing: Taming Cancer’s Resistance with Human Serum Albumin? Int J Nanomedicine. 2025Mar;19(20):3493–525.
60. Greenwald RB, Choe YH, McGuire J, Conover CD. Effective drug delivery by PEGylated drug conjugates. Adv Drug Deliv Rev. 2003Feb 10;55(2):217–50.
61. Kumari P, Ghosh B, Biswas S. Nanocarriers for cancer-targeted drug delivery. J Drug Target. 2016Mar 15;24(3):179–91.
62. Navas F, Chocarro-Calvo A, Iglesias-Hernández P, Fernández-García P, Morales V, García-Martínez JM, et al. Promising Anticancer Prodrugs Based on Pt(IV) Complexes with Bis-organosilane Ligands in Axial Positions. J Med Chem. 2024Apr 9;67(8):6410–24.
63. Han X, Sun J, Wang Y, He Z. Recent advances in platinum (IV) complex-based delivery systems to improve platinum (II) anticancer therapy. Med Res Rev. 2015;35(6):1268–99.
64. Hussein HA, Kassim MNI, Maulidiani M, Abas F, Abdullah MA. Cytotoxicity and 1H NMR metabolomics analyses of microalgal extracts for synergistic application with Tamoxifen on breast

cancer cells with reduced toxicity against Vero cells. Heliyon. 2022Mar 1;8(3):e09192.
65. Frislev HS, Boye TL, Nylandsted J, Otzen D. Liprotides kill cancer cells by disrupting the plasma membrane. Sci Rep. 2017Nov 9;7(1):15129.
66. Hassanin I, Elzoghby A. Albumin-based nanoparticles: a promising strategy to overcome cancer drug resistance. Cancer Drug Resist. 2020;3(4):930.
67. Kızılşahin S, Nalbantsoy A, Karabay Yavaşoğlu NÜ. In vitro synergistic efficacy of conjugated linoleic acid, oleic acid, safflower oil and taxol cytotoxicity on PC3 cells. Nat Prod Res. 2015Feb 16;29(4):378–82.
68. Broadfield LA, Pane AA, Talebi A, Swinnen JV, Fendt SM. Lipid metabolism in cancer: New perspectives and emerging mechanisms. Dev Cell. 2021May 17;56(10):1363–93.
69. Kuche K, Yadav V, Dharshini M, Ghadi R, Chaudhari D, Date T, et al. Synergistic anticancer therapy via ferroptosis using modified bovine serum albumin nanoparticles loaded with sorafenib and simvastatin. Int J Biol Macromol. 2023Dec 31;253(Pt 8):127254.
70. Miyamoto T, Domoto R, Sekiguchi F, Kamaguchi R, Nishimura R, Matsuno M, et al. Development of hepatic impairment aggravates chemotherapy-induced peripheral neuropathy following oxaliplatin treatment: Evidence from clinical and preclinical studies. J Pharmacol Sci. 2022Mar 1;148(3):315–25.